Applied Acoustics 229 (2025) 110392

Contents lists available at ScienceDirect

Applied Acoustics

journal homepage: www.elsevier.com/locate/apacoust

A passive, blade-mounted ultrasonic bat deterrent for wind turbines

Zhangming Zeng [a], Szu-Fu Huang [b], William N. Alexander [b], Anupam Sharma [a,*]

[a] Department of Aerospace Engineering, Iowa State University, 537 Bissell Road, Ames, 50011, IA, USA
[b] Department of Aerospace and Ocean Engineering, Blacksburg, 24061, VA, USA

ABSTRACT

A novel aerodynamic-whistle-based ultrasonic tone generator is proposed that has the potential to serve as a bat deterrent when installed on wind turbine rotor blades. The device uses blade-relative flow to excite resonance in cavities that are geometrically tailored to generate tones at the desired ultrasonic frequencies. A comprehensive experimental and numerical study is presented wherein two such deterrent designs are investigated. Experiments are performed in an anechoic wind tunnel where the deterrents are mounted on a blade section with the NACA 0012 profile. Measurements show that the deterrents produce the desired tonal spectrum when the tunnel flow speed exceeds a threshold value. There is also a maximum flow speed above which the deterrents do not generate tones. Variations with flow speed and blade angle of attack are investigated. Acoustic beamforming is used for source localization with partial success.

The compressible unsteady Reynolds-averaged Navier-Stokes equations are solved with the SST $k-\omega$ turbulence model to simulate the aeroacoustics of the deterrents. Two-dimensional simulations capture the tonal frequencies and the trends with flow speed and blade angle of attack observed in the experiments. Three-dimensional simulations are performed with span-periodic boundaries for two deterrent configurations – one with one resonator modeled and another with two resonators modeled. The flow unsteadiness is higher in the two-resonator configuration; however, the unsteady pressures in the two resonators are nearly out of phase. The Ffowcs Williams-Hawkings acoustic analogy is used to compute far-field acoustics. The simulations capture the tonal sound pressure levels at the fundamental frequency and the second harmonic.

1. Introduction

The US has an installed wind capacity of 140 GW (6% of its total electric supply). The national goal is 40% wind-based electricity, with a projected annual expansion of 66 GW per year over the next decade. This growth will partially be propelled by enhancements in turbine and wind farm design (e.g., [1,2]) that are enabled by novel numerical techniques such as [3–7]. However, achieving this tremendous growth of wind as a truly clean and renewable energy resource requires addressing its adverse ecological impacts, particularly on bats.

Wind energy is one of the largest sources of anthropogenic mortality in bats [8,9] and is considered one of the largest sources of direct mortality for some bat species [10]. Estimates of annual turbine-related bat fatalities are in the hundreds of thousands [11,12], and annual bat fatality per wind turbine can be as high as fifty [13,14], although site-to-site variability in fatality rate is quite large. Combined with significant existing environmental risks that bats face, such as White-nose Syndrome, which has led to the death of over 5 million bats in eastern North America since its identification in New York in 2006 [15], wind-related bat mortality is driving certain species towards extinction [16–18].

Multiple strategies are currently being pursued to mitigate bat fatalities at wind turbines. These strategies encompass: a) operational mitigation [19–21], involving the reduction of power generation at low wind speeds, and b) deterring bats from wind farms using ultrasonic deterrents [20,22,23], ultraviolet lights [24], and/or application of textured paints on turbine towers [25]. A big drawback of operational mitigation is the reduced energy capture due to power curtailment at low wind speeds, which can render it cost-prohibitive in many circumstances. Therefore, few companies implement this strategy unless mandated by local rules and regulations. In contrast, bat deterrence technologies do not necessitate curtailment and represent an efficient alternative. Initial trials of such deterrents have shown promise [20]; however, their long-term efficacy still requires conclusive validation. Combinations of different technologies, such as curtailment and ultrasonic deterrents, have also been explored [26].

Bats navigate and forage using echolocation at ultrasonic frequencies. Consequently, they avoid regions where their echolocation signals are jammed or overwhelmed by high-amplitude ultrasound. Schirmacher [27] showed that the deterrence signal need not be broadband; a tonal spectrum also provides bat deterrence capability. Compared to broadband, a tonal signal/spectrum concentrates its acoustic energy into select frequencies, allowing for the augmentation of the intensity of these tones and enabling a longer range. Also, deterrents that generate a tonal spectrum require less power and are a plausible choice for

* Corresponding author.
E-mail address: sharma@iastate.edu (A. Sharma).

https://doi.org/10.1016/j.apacoust.2024.110392
Received 2 January 2024; Received in revised form 17 October 2024; Accepted 5 November 2024
Available online 18 November 2024
0003-682X/© 2024 Elsevier Ltd. All rights are reserved, including those for text and data mining, AI training, and similar technologies.

"passive" operation. By passive operation, we imply that the deterrent is driven by blade-relative airflow and does not require any external power source (e.g., electricity or compressed air).

Currently employed ultrasonic deterrents utilize electromechanical transducer-driven speakers, as described in Horn et al. [28], to produce ultrasound. The Bat Deterrent System (BDS) developed by NRG Systems [27] is an example of such a deterrent. One unit of the NRG BDS consists of six sub-arrays, each generating ultrasonic tones at prescribed frequencies via multiple transducers. Such a unit can generate tones distributed between 20 kHz to 50 kHz, which covers the echolocation frequencies of most bat species in the USA. Schirmacher [27] verified the six-tone BDS to be effective in reducing bat fatality. In their field study, Weaver et al. [23] found that ultrasonic deterrents significantly reduced fatalities in certain bat species.

The electromechanical ultrasonic deterrents have the following limitations: a) they rely on external power, constraining their possible placement to the turbine nacelle and tower, b) maintenance challenges arise due to susceptibility to rain/water damage, leading to increased operational costs, and c) atmospheric absorption prevents the deterrence signal (ultrasound) from reaching the blade tips, rendering them ineffective in regions with elevated bat fatality risks resulting from high blade speeds.

Aerodynamic ultrasonic deterrents have also been pursued. Romano et al. [22] tested a device in which compressed air was accelerated in a converging-diverging nozzle and ejected as a supersonic jet. The turbulence in the jet shear layer generates broadband noise in the ultrasonic frequency range ($20-100$ kHz). Aerodynamic whistling, or flow-excited resonance, is an effective way of generating tonal (ultra)sound. An aerodynamic whistle is a self-sustaining oscillator that generates high-amplitude acoustic tones [29]. The feedback mechanism is the essence of aerodynamic whistles. Based on the feedback mechanism, Chanaud [29] classified aerodynamic whistles into three categories. In Class I whistles, the flow instability provides the feedback directly, whereas the feedback is provided by the sound generator in Class II whistles, and by the resonator/sound reflector in Class III whistles. Flow-excited resonance is widely observed in nature. A notable illustration of this occurs when a fluid jet moves through a confined area (hole), similar to how humans whistle by directing air through the small gap formed by their lips. This produces what is known as "hole tones," where the mouth's cavity functions as a Helmholtz resonator [30]. Our ability to modify the whistling frequency by altering the shape of the mouth cavity has been experimentally investigated by [31].

Flow over a cavity is also a common source of aerodynamically generated sound/noise. Cavity noise can be classified as either a Class II or a Class III whistle. Gloerfelt [32] identified the possible mechanisms of cavity noise to be: (i) Rossiter modes [33], which occur because of the feedback from the acoustic waves generated when the free shear layer over the cavity interacts with its downstream edge, (ii) Helmholtz resonance due to the compressibility of the fluid in the cavity, and (iii) standing-wave resonance in the cavity (depth, longitudinal and spanwise modes). Rossiter modes are associated with Class II whistles, while Helmholtz resonance and standing-wave resonance are Class III whistles. Multiple resonance mechanisms co-exist in some cases, e.g., Helmholtz resonance can exist simultaneously with standing wave resonance in a cavity [34].

While typically used to generate human-audible sound, aerodynamic whistles can be tailored to generate ultrasound [36]. The advantages of aerodynamic-whistle-based ultrasonic deterrents include design simplicity (no moving parts), low cost, and the potential for generating high-amplitude ultrasound with minimal power (in terms of air supply) requirements.

In this work, we investigate aerodynamic-whistle-based passive ultrasonic bat deterrents for wind turbines. These deterrents are intended to be mounted on turbine blades and use the blade-relative air flow to excite resonance and generate tones at ultrasonic frequencies. In contrast, "active" aerodynamic whistles require a compressed air supply; we have investigated active aerodynamic whistles in prior works [37,35,38]. Besides the ability to operate passively using blade-relative airflow, another key advantage of blade-mounted deterrents is that they are located at/near the source of bat fatalities [39,40], minimizing the distance the signal (ultrasound) produced by the deterrents has to travel. This is advantageous because atmospheric absorption heavily attenuates high frequencies. Modern utility-scale wind turbine rotor blades are reaching lengths upward of 120 m. It is nearly impossible for high ultrasonic frequencies to travel such distances and protect the blade tips from deterrents mounted on the turbine nacelle/hub.

Two passive whistle designs targeting fundamental frequencies 20 kHz and 10 kHz are designed, prototyped, and investigated. The onset flow speed for cavity oscillations in the resonators is not know a priori. The 20 kHz resonator, being smaller, is expected to have a higher onset flow speed (see [41]). The 10 kHz design is a risk mitigation measure – to ensure that resonance is observed in the measurements given the speed limitation of the wind tunnel (described in Section 3.1).

Systematic numerical and experimental analyses are carried out to quantify the acoustic performance of the whistles, assess the impact of the whistles on the aerodynamic performance of the blade section where they are mounted, and identify the sound generation mechanisms. The experiments are conducted in the Virginia Tech Stability Wind Tunnel in its hemi-anechoic configuration. The measurements show that the passive whistle deterrent can readily generate the desired frequency spectrum under typical operating conditions of utility-scale wind turbines. Numerical predictions of the radiated sound are obtained by coupling the near-field computational fluid dynamics solution with an acoustic analogy. Based on our experimental and numerical results, the proposed deterrent design has the potential for future field deployment.

2. Passive whistle design

The passive whistle is an adaptation of the active whistle described in [35]. Figure 1a shows a computer model of the active whistle. In the active whistle, compressed air is forced into a channel where it passes over two identical resonating chambers facing each other. Zeng and Sharma [35] showed that Helmholtz resonance dominates sound generation and the two resonators oscillate out-of-phase, nearly canceling the sound radiation at the fundamental frequency (f_R) of a single resonator and the odd harmonics ($3\times f_R$, $5\times f_R$, …). Sound radiation is therefore limited to the even harmonics ($2\times f_R$, $4\times f_R$, …) of the fundamental frequency.

The passive whistle is designed to be embedded into the airfoil (Fig. 1b) or on a sleeve that can be attached to the airfoil (Fig. 2c). The resonating chamber in the passive whistle is similar to that in the active whistle, but it is exposed directly to the external flow over the airfoil rather than being confined to a channel. There is no "opposing" resonator to provide an out-of-phase signal and cancel out the odd harmonics. Since the fundamental tone is not canceled, the geometry of the chamber has to be scaled to ensure ultrasonic radiation, i.e., the fundamental frequency of the resonator has to be increased to lie in the ultrasonic range. This leads to a reduction in resonator size. The key geometric parameters of the passive whistle are shown in Fig. 1c.

2.1. Designs for wind tunnel testing

Two passive whistle designs are developed for experimental evaluation: (1) a high-frequency (HF) design and (2) a low-frequency (LF) design. Table 1 lists the design parameters for the two passive whistle configurations and theoretical estimates of their Helmholtz resonance frequencies. Note that the fundamental tone of the LF design is in the human-audible frequency range and, hence, does not qualify as an ultrasonic whistle/deterrent. The whistles are located at 4% chord downstream of the blade leading edge and are oriented such that the openings of the resonating chambers are aligned with the local airfoil surface. The

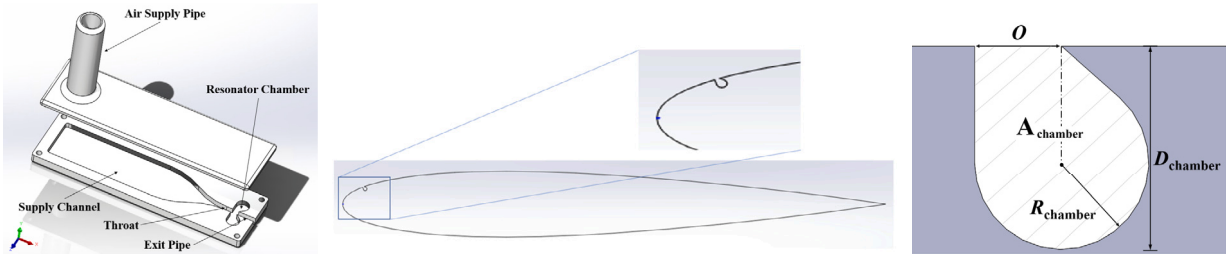

(a) Active whistle (b) Passive whistle embedded in an airfoil (c) Design parameters

Fig. 1. Computer drawings of the active and passive whistle designs: (a) active whistle design of Zeng and Sharma [35], and (b) the proposed passive whistle embedded in an airfoil near its leading. The geometry of the resonator in the passive whistle is borrowed from the active whistle. The key design parameters of the passive whistle are shown in panel (c); A_{chamber} is the area of the resonating chamber.

Table 1
The design parameters for the two passive whistles that are experimentally evaluated. Theoretical estimates of the Helmholtz resonance frequency (f_R) are also listed for each design. Appendix B of [35] explains how f_R is estimated.

Configuration	D_{chamber} [mm]	R_{chamber} [mm]	O [mm]	A_{chamber} [mm^2]	f_R (kHz)
High frequency (HF)	2.24	0.96	0.96	3.482	29.0
Low frequency (LF)	5.60	2.40	2.40	21.39	11.7

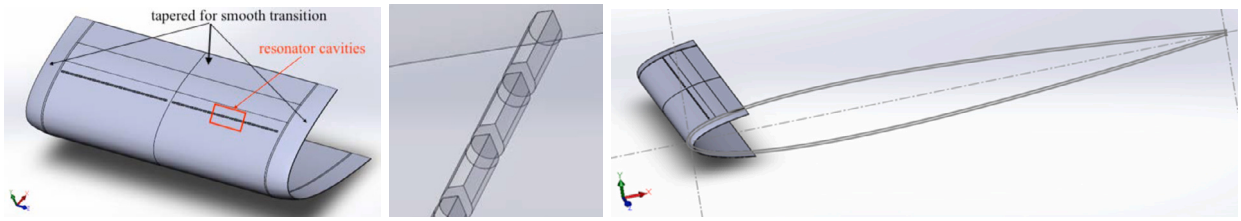

(a) Whistles printed on a sleeve (b) Zoomed view (c) Sleeve mounted on an airfoil

Fig. 2. A computer model of the passive deterrent design: (a) whistles engraved on a sleeve, (b) a zoomed view of the resonating cavities (whistles), and (c) the sleeve fitted on the nose of a blade formed by extruding the NACA 0012 airfoil.

deterrent is formed by repeating these whistles along the span of the blade (Fig. 2).

For the prototypes tested in the Virginia Tech Stability Tunnel (facility description in Section 3.1), the deterrent is engraved on a thin "sleeve" that wraps around the leading edge of the blade model. The deterrents can be directly engraved on the blade, but the sleeve approach was chosen to allow the testing of multiple deterrents on the same baseline blade model. The drag force assists in keeping the sleeve/prototype attached to the blade, which minimizes the risk of the prototype tearing off the blade and damaging the wind tunnel. The leading-edge geometry of the sleeve is obtained by normal extrusion of the original airfoil shape with tapering at the edges to ensure a smooth transition to the baseline blade geometry. Figure 2c demonstrates the sleeve design and how it fits the blade at the leading edge.

For use on existing wind turbine blades, where engraving the deterrents on the blades would be expensive and risky, and having a sleeve that goes around the leading edge can be costly and might adversely impact the blade's aerodynamic performance, the following approach can be taken. The deterrents can be 3D printed on a small substrate that follows the local blade surface contour, and the substrate can be glued or fastened to the blade.

Figure 3 shows the deterrent prototypes fabricated via 3D printing using acrylic. One row with 48 resonator slots was printed on both sides of the sleeve (corresponding to the suction and pressure sides of the blade). Each resonating cavity is 5 mm long in the span direction for the HF design and 7 mm long for the LF design, with a 1 mm gap between adjacent cavities. This design approach was chosen over a single cavity spanning the entire length of the deterrent to prevent spanwise flow and to avoid additional, low-frequency resonant modes corresponding to standing waves in the span direction.

Figure 3b shows the resonator cavities engraved on the sleeve. The sleeve is designed to fit the blade model in the Virginia Tech Stability Wind Tunnel (see Fig. 4a). Due to the limitation of the 3D printer, each passive deterrent was printed in four parts (two with resonator slots engraved on them and two tapered ends), which were later assembled before mounting on the blade model in the wind tunnel. The 3D printed parts were hand polished using 2000-grit sandpaper for a smooth surface finish.

3. Methods

3.1. Experimental methodology

Experiments were conducted in the Virginia Tech Stability Wind Tunnel to evaluate the acoustic performance of the passive deterrents. The wind tunnel has a 1.83 m × 1.83 m test section and was set up in its hemi-anechoic configuration (see Fig. 4a). The port wall of the facility is made of a single layer of tensioned Kevlar fabric backed by an anechoic chamber. The starboard wall is a flat, non-porous aluminum wall on which the array is mounted. The test section's floor and ceiling upstream and downstream of the blade model are acoustically treated. The blade is mounted at the center of the test section, and the deterrent (marked as "LE Device" in Fig. 4a) is mounted at the mid span of the blade. The airfoil used in these experiments is two-dimensional, extended 1.83 m from the floor to the ceiling of the test section, and is constructed with fiberglass. The two-dimensional airfoil follows a nominal NACA 0012

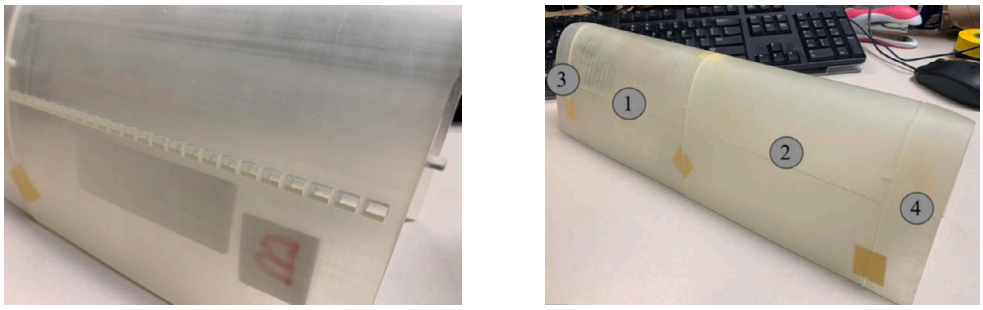

(a) (b)

Fig. 3. A 3D printed passive deterrent on a sleeve. The deterrent is printed in four parts due to the size limitation of the 3D printer. (a) A zoomed view of the resonating cavities (resonators), and (b) the assembled sleeve with the resonators engraved in it.

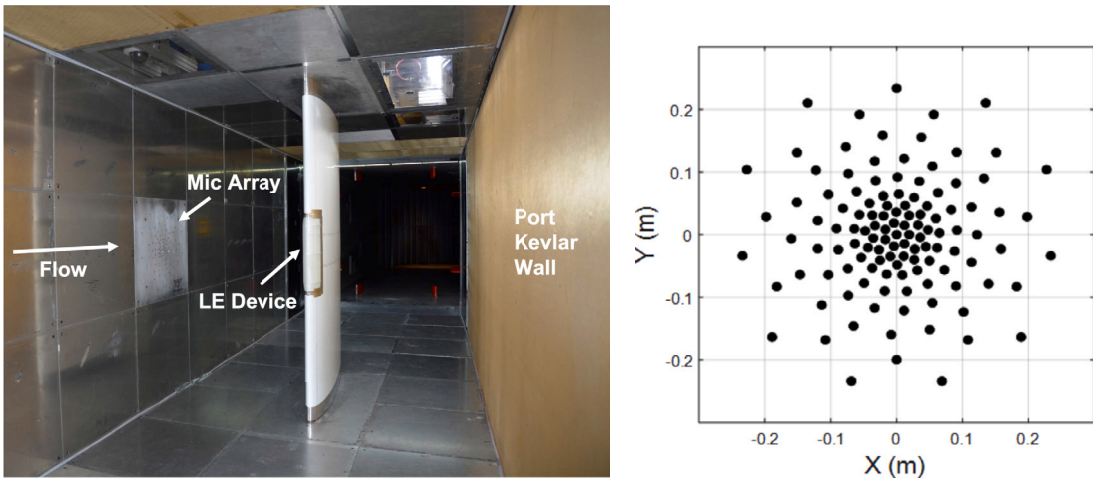

(a) The Virginia Tech Stability Wind Tunnel (b) Microphone array

Fig. 4. Experimental setup in the Virginia Tech Stability Wind Tunnel. (a) A blade section (extruded NACA 0012 airfoil is used here) is mounted in the middle of the anechoic test section. The passive bat deterrent (labeled 'LE Device') is installed on the blade's leading edge. An array of microphones is mounted flush with the starboard wall to measure the radiated ultrasound and to locate its source via beamforming. The port wall is formed with tensioned Kevlar, which allows the acoustic waves to radiate out while retaining the flow in the tunnel. (b) The 120-channel high-frequency microphone array for measuring radiated ultrasound.

profile with a 914 mm chord length. The Stability Tunnel can operate at freestream speeds up to 80 m/s but was limited to 60 m/s for this experiment. The maximum blade tip speed for land-based utility-scale wind turbines has historically been limited to be in the range $75-80$ m/s [42]. Hence, a 60 m/s blade speed would occur at a normalized radius, r/r_{tip} between 0.75 and 0.8 for such a turbine operating at its design point.

The sound signal generated by the deterrent is measured using a 120-channel high-frequency microphone array (Fig. 4b). The array is mounted on the starboard side of the test section in individual sockets which hold the microphones behind wire mesh coverings flush with the tunnel wall. This array comprises microphones arranged in logarithmic spirals with a maximum aperture of 0.5 m. The array employs GRAS 46BD-FV microphones with a frequency response between 5 kHz to 70 kHz within ± 2 dB. Szoke et al. [43] provides a complete description of this array.

3.2. Measured data processing

Data is acquired for 32 seconds for each microphone in the array at a 374.4 kHz sampling rate. The cross-spectral matrix is obtained using a signal length of $14,976$ samples with a 50% overlap rate and a Hanning window. Acoustic maps are generated using conventional delay and sum beamforming with convection and atmospheric attenuation corrections. Integrated spectra are produced by integrating an area 0.643 m $\times$ 0.592 m in the streamwise and vertical directions respectively, centered about the mid-span of the airfoil leading edge. The deterrent is located at a streamwise distance of 0.0415 m upstream from the center of the microphone array, centered at the mid-span of the airfoil, and between spanwise locations -0.148 m and 0.148 m. The airfoil, lying along the centerline of the test section, is at a distance of 0.92 m from the plane of the microphone array.

The beamform integrated spectra show multiple equispaced (in frequency) pure tones above the relatively broad peaks at the harmonics of the resonance frequency of the deterrents (see Fig. 23). Appendix A presents a plausible explanation for the existence of these unexpected tones. We hypothesize that these tones are an artifact of measuring sound in the semi-anechoic (as opposed to fully anechoic) configuration of the wind tunnel; the side wall on which the microphone array is mounted is an acoustically reflecting surface. To remove these artificial tones, we convolve the data via a Gaussian filter with a half-width of 150 Hz and present only the filtered results in the paper.

3.3. Numerical methodology

Computational aeroacoustics (CAA) simulations use a two-step process wherein the acoustic sources are first obtained via unsteady computational fluid dynamics (CFD) simulations. The radiated acoustic intensity and directivity are subsequently computed via the Ffowcs Williams-Hawkings acoustic analogy. We use the STAR-CCM+ software

for the simulations. The numerical results supplement the radiating farfield acoustic measurements with near-field flow and acoustics information to enable a comprehensive understanding of the flow and acoustic mechanisms involved. The simulations are performed in two and three spatial dimensions. The two-dimensional (2-D) simulations are used to study the acoustic performance of different resonator sizes at different freestream flow speeds (V_∞) and angles of attack (α). The three-dimensional (3-D) simulations are used for (a) verification with experiments, (b) investigating the interaction between adjacent resonators in a deterrent, and (c) predicting the directivity of the radiating acoustic field.

Fluid flow is governed by the conservation of mass, momentum, and energy equations. This system of equations with an equation of state is called the Navier-Stokes (N-S) equations. We solve the unsteady Reynolds-averaged Navier-Stokes (uRANS) equations, obtained by short-time, density-weighted (Favre) averaging the Navier-Stokes equations. Favre averaging results in unresolved turbulence (closure) terms, which are modeled using a turbulence closure model. A $k-\omega$ turbulence model is used in this work wherein transport equations for the turbulence kinetic energy (k) and specific dissipation rate (ω) are solved with appropriately tuned production and dissipation terms.

The density-weighted, short-time averaged N-S equations are

$$\frac{\partial \bar{\rho}}{\partial t} + \frac{\partial}{\partial x_j}(\bar{\rho}\tilde{u}_j) = 0, \tag{1}$$

$$\frac{\partial}{\partial t}(\bar{\rho}\tilde{u}_i) + \frac{\partial}{\partial x_j}(\bar{\rho}\tilde{u}_i\tilde{u}_j) = -\frac{\partial \bar{p}}{\partial x_i} + \frac{\partial}{\partial x_j}(\bar{\tau}_{ij} - \overline{\rho u_i'' u_j''}), \tag{2}$$

$$\frac{\partial}{\partial t}(\bar{\rho}c_p\tilde{T}) + \frac{\partial}{\partial x_j}(\bar{\rho}c_p\tilde{T}\tilde{u}_j) = \frac{\partial \bar{p}}{\partial t} + \tilde{u}_j\frac{\partial \bar{p}}{\partial x_j} + \overline{u_j''\frac{\partial p}{\partial x_j}} + \frac{\partial}{\partial x_j}\left(\kappa\frac{\partial \tilde{T}}{\partial x_j} + \kappa\frac{\partial \bar{T}''}{\partial x_j} - c_p\,\overline{\rho u_j'' T''}\right) + \bar{\Phi}, \tag{3}$$

where the shear stress term $\bar{\tau}_{ij}$ can be written as

$$\bar{\tau}_{ij} = \mu\left[\left(\frac{\partial \tilde{u}_i}{\partial x_j} + \frac{\partial \tilde{u}_j}{\partial x_i}\right) - \frac{2}{3}\delta_{ij}\frac{\partial \tilde{u}_k}{\partial u_k}\right] + \mu\left[\left(\frac{\partial \overline{u_i''}}{\partial x_j} + \frac{\partial \overline{u_j''}}{\partial x_i}\right) - \frac{2}{3}\delta_{ij}\frac{\partial \overline{u_k''}}{\partial u_k}\right], \tag{4}$$

and the dissipation function $\bar{\Phi}$ can be written as

$$\bar{\Phi} = \overline{\tau_{ij}\frac{\partial u_i}{\partial x_j}} = \bar{\tau}_{ij}\frac{\partial \tilde{u}_i}{\partial x_j} + \overline{\tau_{ij}\frac{\partial u_i''}{\partial x_j}}. \tag{5}$$

In the above, the overline ($\bar{}$) denotes short-time-averaging and the tilde ($\tilde{}$) represents density-weighted, time-averaging. The superscript ($''$) refers to the fluctuation of the mass-averaged variables. To close the system of equations, the Reynolds stress tensor $-\overline{\rho u_i'' u_j''}$ and some other terms (e.g., $\partial(\overline{\rho u_j'' T''})/\partial x_j$) have to be modeled. In this research, the shear stress transport (SST) $k-\omega$ model of Menter [44] is used.

3.3.1. Acoustic prediction

The Ffowcs Williams-Hawkings (FW-H) acoustic analogy is used to predict acoustic propagation to the farfield from the near-field time-resolved flow data obtained from CFD. The FW-H formulation can be expressed in the following differential form.

$$\left(\frac{\partial^2}{\partial t^2} - c_o^2\frac{\partial^2}{\partial x_i \partial x_i}\right)\left(H(f)\rho'\right) = \frac{\partial^2}{\partial x_i \partial x_j}\left(T_{ij}H(f)\right) - \frac{\partial}{\partial x_i}\left(F_i\delta(f)\right) + \frac{\partial}{\partial t}\left(Q\delta(f)\right) \tag{6}$$

where,

$$T_{ij} = \rho u_i u_j + P_{ij} - c_o^2\rho'\delta_{ij},$$
$$F_i = (P_{ij} + \rho u_i(u_j - v_j))\partial f/\partial x_j, \text{ and} \tag{7}$$
$$Q = (\rho_o v_i + \rho(u_i - v_i))\partial f/\partial x_j.$$

P_{ij} is the compressive stress tensor, f is the function that describes the integration surface, and $H(f)$ is the Heaviside function. Integration of Eq. (6) results in an unsteady mass addition (monopole) term corresponding to Q, an unsteady force (dipole) term corresponding to F_i, and an unsteady volume (quadrupole) term corresponding to T_{ij}. The flow speed is small in the simulations presented here, and the volume integral term corresponding to T_{ij} can be ignored. Therefore, only the surface integrals are required to be computed. The surface used for acoustic prediction using such an acoustic analogy is often called a Kirchoff surface. A "porous" Kirchoff surface enclosing the acoustic sources is used here that allows flow to pass through. Figure 5 shows the Kirchoff surface used in the current predictions.

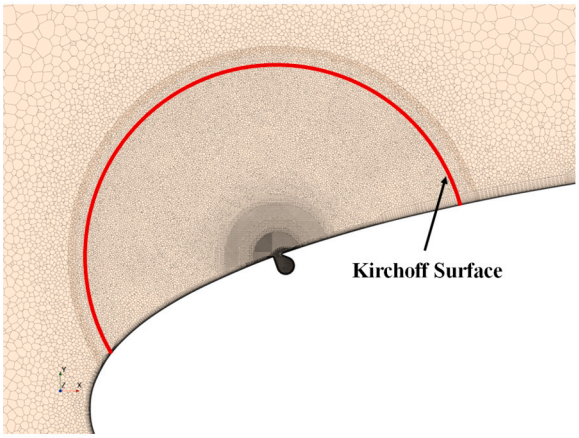

Fig. 5. The integration (Kirchoff) surface used in the present work to predict farfield acoustics using the FW-H acoustic analogy.

Table 2
Test matrix to evaluate the passive ultrasonic deterrents. The baseline blade (Base) is the NACA 0012 model without any deterrent installed; the HF and LF are the deterrent configurations from Table 1. The chord-based Reynolds number (Re_c) varies with the freestream flow speed (V_∞).

V_∞ [m/s]	α [deg]	Configuration	Re_c ($\times 10^6$)
30	0	Base, LF	1.67
35	0	Base, LF	1.94
40	0	Base, LF	2.22
45	0	Base, LF	2.50
50	0	Base, LF	2.75
55	0	Base, HF, LF	3.02
60	0, 2, 4	Base, HF, LF	3.27

Atmospheric absorption Atmospheric absorption effects on sound propagation must be accounted for in the numerical predictions to compare with experimental measurements. The atmospheric absorption coefficients are calculated using the ANSI standard [45,46] for the tonal frequencies in the predicted spectra with the temperature, relative humidity, and pressure set as 293 K, 50% and 1 atm, respectively.

4. Experimental measurements

The baseline blade uses the NACA 0012 profile that is extruded along the span. The two deterrent configurations, HF and LF (see Table 1), and the baseline blade were tested in the Virginia Tech Stability Wind Tunnel to characterize the acoustic performance of the deterrents for varying freestream flow velocity (V_∞) and blade angle of attack (α). The full test matrix is provided in Table 2.

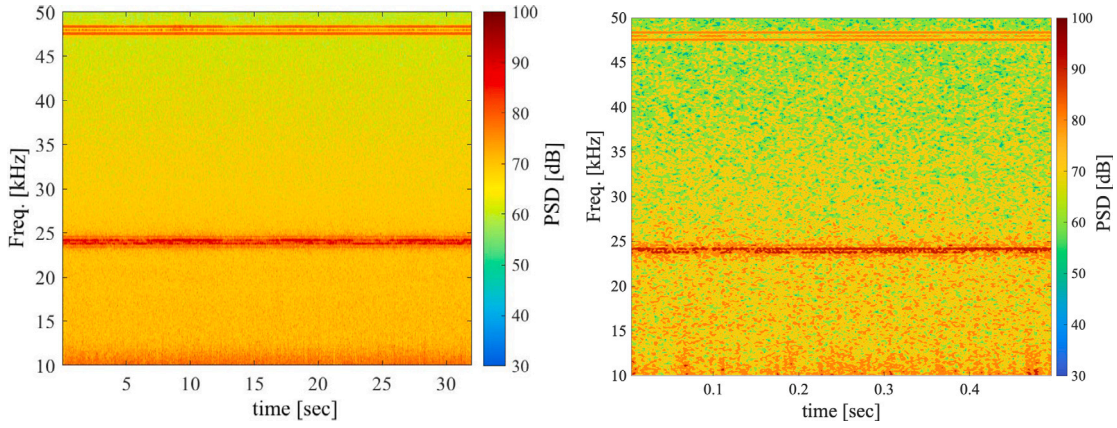

Fig. 6. Spectrograms of acoustic pressure for the HF deterrent measured by the center microphone of the phased array over a long time (a) and over a short time (b). Steady acoustic radiation is observed. Operating conditions: $V_\infty = 60$ m/s and $\alpha = 0°$.

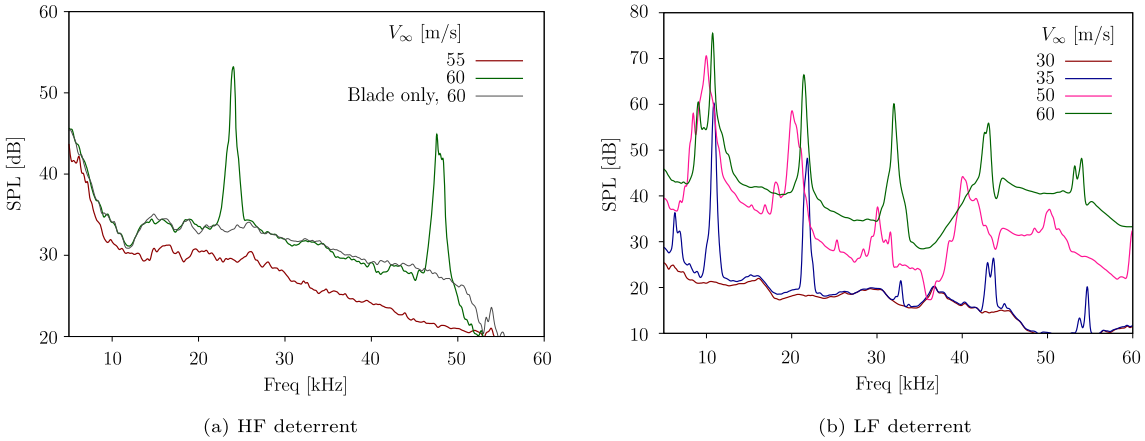

Fig. 7. Variation with flow speed (V_∞) of the filtered SPL spectra for the (a) HF deterrent and the (b) LF deterrent. The gray line in panel (a) is the filtered spectrum of the acoustic radiation from the baseline blade without any deterrent installed. Filtering broadens the spectral peaks and makes the tonal SPL values look lower than they are.

Figure 6 plots the spectrogram of acoustic radiation from the HF deterrent at $V_\infty = 60$ m/s and $\alpha = 0°$. The signal is acoustic pressure measured at the center of the microphone array. Steady tones are observed at ~ 24 and 48 kHz. No deterministic modulation in frequency or amplitude is observed.

4.1. Variation with flow speed

Figure 7 plots the filtered sound pressure spectra at different flow speeds (V_∞) for the HF and LF deterrents. The spectra are shown only for selected values of V_∞. The deterrents do not produce sound below a critical flow speed, which is deterrent-specific. This critical (minimum) speed is called the 'onset' speed. The onset flow speed is a function of the geometry (size) of the resonator, with the larger resonator having a smaller $V_{\infty,\min}$. These observations are consistent with prior experiments [41,47,48]. The onset speeds for the HF and LF deterrents are between 55 – 60 m/s and 30 – 35 m/s, respectively (see Fig. 7).

Beyond the onset speed, the HF deterrent generates a high-amplitude tone at the fundamental frequency of 23.8 kHz and the second harmonic at 47.6 kHz. Higher harmonics likely exist, but the microphones do not capture sound above 60 kHz. The noise radiation from the baseline blade (no deterrent) at $V_\infty = 60$ m/s is shown in gray in Fig. 7a. Other than the tones at the fundamental and the second harmonic of the HF resonators, the radiated acoustic spectrum with the deterrent installed follows that of the baseline blade, suggesting that the sleeve used to mount the deterrents does not introduce significant additional noise.

No radiation is observed at $V_\infty = 30$ m/s (which is below the onset speed) for the LF deterrent. At $V_\infty = 35$ m/s, the fundamental tone for the LF deterrent (~ 10.8 kHz) and several higher harmonics are observed. There is also discernible acoustic radiation at this V_∞ in a sub-harmonic of the fundamental, at around 5.6 kHz. As V_∞ increases to 60 m/s, the sub-harmonic tone subsides, and the spectrum shows prominent tones at the fundamental and higher harmonics.

4.2. Variation with angle of attack

The angle of attack is varied by pitching the blade about the quarter-chord line. Figure 8 plots the SPL spectra of the HF and LF deterrents for three angles of attack, $\alpha = 0°$, 2°, and 4°. It should be noted that α is defined for the blade; the resonators are engraved on both sides of the sleeve that wraps around the leading edge of the blade. Hence, one set of resonators is on the suction side while the other is on the pressure side of the blade. The acoustic array is on the Starboard side of the tunnel. As α increases, the blade leading edge is tilted towards the microphone array. Blade pitching, therefore, affects not only the aerodynamics but also the distance and the angle between the acoustic source (deterrent) and the microphone array. On average, the increase in α from 0° to 4° increases the radiated acoustic intensity. This is due to the increase in local flow speed due to the acceleration of the flow around the airfoil leading edge

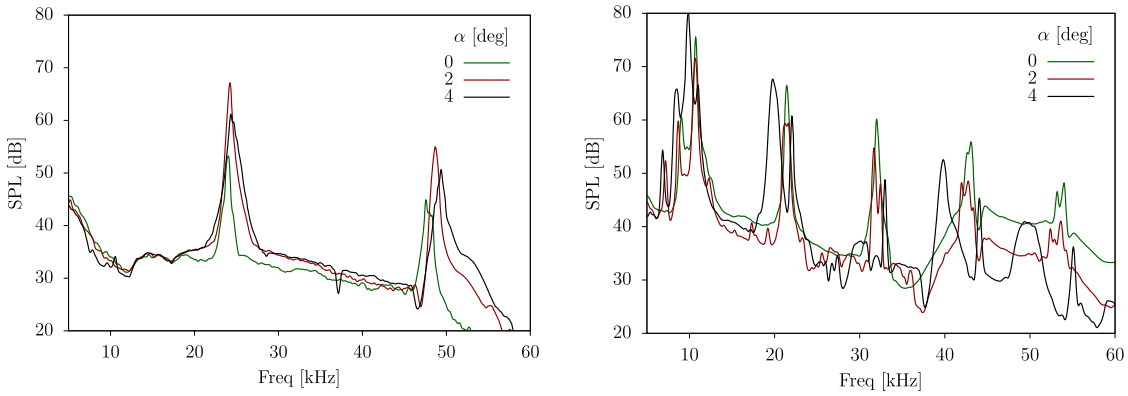

(a) HF deterrent (b) LF deterrent

Fig. 8. Variation with blade angle of attack (α) of the filtered SPL spectra for the (a) HF deterrent and the (b) LF deterrent, at $V_\infty = 60$ m/s.

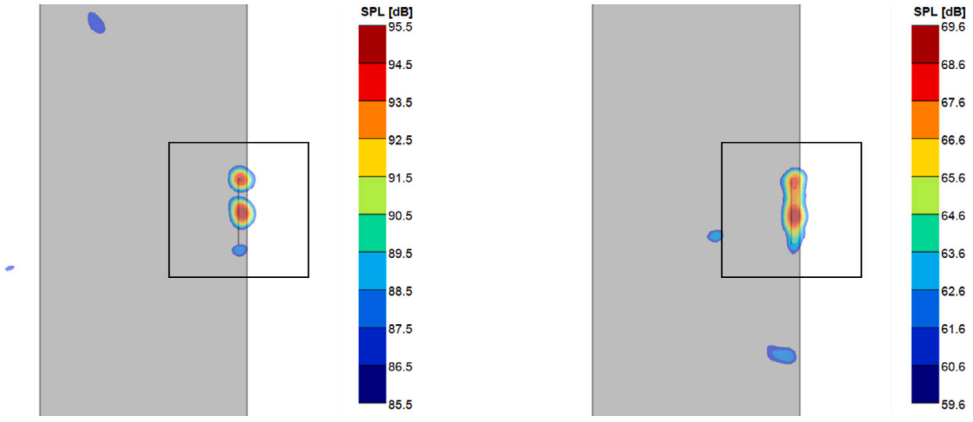

(a) 10.6 kHz (b) 11.2 kHz

Fig. 9. Beamform maps at two frequencies around the fundamental frequency of the LF deterrent superimposed on the planform of the airfoil (gray box). The black rectangle shows the integration region used to obtain the acoustic spectra. $V_\infty = 60$ m/s and $\alpha = 0°$.

on the suction side of the blade with increasing α. There is also a small increase (< 0.3 kHz) in the peak frequency for the HF deterrent with increasing α. This is consistent with the numerical results presented in Section 5.2; see Fig. 16, which shows an increase in the fundamental resonance frequency with flow speed.

For the LF deterrent, increasing α leads to the generation of non-harmonic tones. Even after filtering, several peaks are observed around the broad spectral peaks at harmonics of the resonance frequency (see Fig. 8b). While the trend of increasing acoustic intensity with α is apparent, the frequency shift is difficult to ascertain for the LF deterrent due to the several additional peaks that vary with the size of the Gaussian filter used. The measurements show that both deterrents generate tones at the desired frequencies for the three α values considered.

4.3. Beamform maps

Beamform maps provide a visual illustration of the physical location of acoustic sources. The beamform maps are computed using 1/12th octave band spectra to reduce uncertainty. Figure 9 shows the beamform maps for the LF deterrent at $V_\infty = 60$ m/s and $\alpha = 0°$. Two maps are shown with center frequencies 10.6 kHz and 11.2 kHz; the fundamental frequency of the resonators in the LF deterrent is ~ 10.8 kHz. At 10.6 kHz, the map shows three point sources, one near the center and two at the span ends of the deterrent (Fig. 9a). At 11.2 kHz frequency, the map shows a strong source across the span of the deterrent. The deterrent is much louder (at least 10 dB) than the noise produced by the airfoil and the tunnel at these frequencies. Therefore, the only acoustic sources in the maps are at the deterrent location. Similar results were observed at higher α for the LF deterrent.

The beamform maps for the HF deterrent (Fig. 10) do not show a clear source location, which was unexpected because the integrated spectra (see Figs. 7a and 8a) show clear tones at the harmonics of the resonance frequency. Appendix B explains why the acoustic source locations are not accurately identified in the beamform maps, particularly for the HF deterrent.

5. Computational results

Numerical simulations are performed to supplement the measurements. The baseline blade and the HF deterrent are simulated. Two-dimensional (2-D) simulations are performed first to assess the impact of the deterrent on the aerodynamic performance of the blade/airfoil. The 2-D simulations are also used to evaluate the acoustic performance of the passive whistle; their results are compared qualitatively with measurements. While acoustic radiation is a 3-D phenomenon, (ultra)sound generation in the passive whistles is primarily two-dimensional; 3-D effects on acoustic sources are investigated in Section 5.3. Appendix C summarizes the results of a mesh sensitivity study to identify the optimum mesh spacing and time step for the simulations; the baseline mesh (see Appendix C) and $\Delta t = 2.5E-07$ are used for the simulations.

Two-dimensional simulations are performed over a range of free-stream flow speeds (V_∞), corresponding to the blade speed in the outer 50% of a typical utility-scale wind turbine rotor. Variation with airfoil angle of attack (α) is also evaluated. Three-dimensional CAA simula-

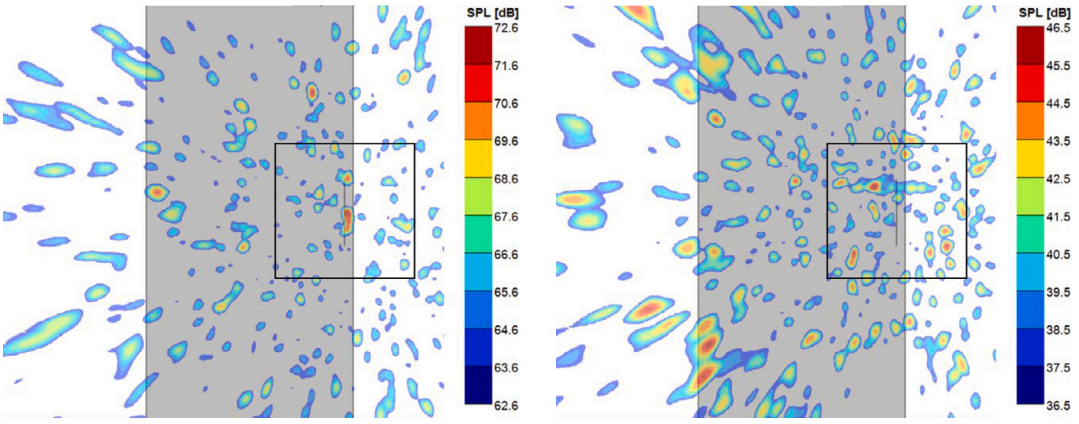

(a) 23.6 kHz (b) 25.0 kHz

Fig. 10. Beamform maps around the fundamental frequency of the HF deterrent superimposed on the planform of the airfoil (gray box). The black rectangle shows the integration region used to obtain the acoustic spectra. $V_\infty = 60$ m/s and $\alpha = 0°$.

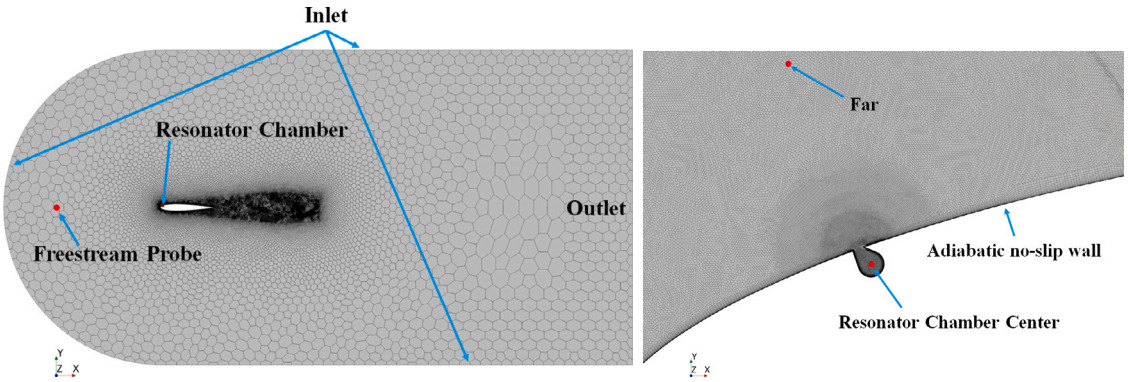

(a) 2D CFD domain (b) resonating cavity/chamber

Fig. 11. The computational mesh used for the 2D simulations. (a) The full computational domain, and (b) a zoomed view of the mesh inside and around the resonating cavity.

tions are then performed to (a) quantitatively compare against acoustic measurements made in the Virginia Tech Stability Wind Tunnel, (b) investigate the three-dimensional aerodynamic and acoustic interactions between adjacent resonators in the passive deterrents, and (c) assess the directivity of the radiated ultrasound.

We first present the 2-D results. Figure 11a shows the computational domain, the mesh, and the boundary conditions used for the simulations. Figure 11b shows a zoomed view of the mesh inside and around the resonating cavity. The resonator is only placed on the suction side of the airfoil (at 4% chord) to reduce the mesh size and the computational cost. Freestream Mach number, flow direction, and stagnation pressure and temperature are specified at the inlet boundaries. Static pressure at the outlet boundary is set to atmospheric pressure. The airfoil surface is treated as a no-slip, adiabatic wall.

5.1. Aerodynamic performance

The aerodynamic influence of the deterrent on the blade is evaluated by comparing the airfoil polars between the baseline and the deterrent configurations. The baseline is the NACA 0012 airfoil, and the HF resonator is used for the deterrent.

Figure 12 compares the lift and drag coefficients (c_l and c_d respectively) and the lift-to-drag ratio (c_l/c_d) between the baseline blade and the deterrent configurations. Also plotted are XFOIL [49] predictions for reference. At small α, the CFD predictions are in good agreement with XFOIL and there is negligible impact on the aerodynamic performance of the blade because of the deterrent. For larger α ($> 8°$), CFD predicts a higher drag value for the baseline blade than XFOIL. At these high α values, the boundary layer is thick near the airfoil's trailing edge and may also be partially separated. Since the objective of this study is ultrasound generation by the passive deterrents, which are mounted near the airfoil leading edge, the mesh is coarsened towards the airfoil trailing edge to save computational time. This could be a reason for the overprediction of drag (c_d) and the underprediction of c_l/c_d in CFD. The accuracy of XFOIL is also questionable at high α when separated flow can occur near the trailing edge. Nevertheless, the CFD predictions show little impact of the deterrent on the aerodynamic performance of the airfoil/blade over the range of α tested.

Figure 13 plots the distributions of coefficients of pressure and skin friction (c_p and c_f respectively) on the airfoil surface at $\alpha = 8.5°$, where c_l/c_d is maximum. Wind turbine rotor blades operate at α corresponding to $\max(c_l/c_d)$ at the design point. CFD and XFOIL results are in good agreement. Moreover, the difference between the results for the baseline blade and the blade with a deterrent installed is negligible. We can, therefore, conclude that these deterrents will not adversely impact the aerodynamic performance of wind turbines if they are engraved into the rotor blades; the aerodynamic impact of the sleeve mounting approach (used in the current laboratory experiments) is not assessed.

5.2. Acoustic performance

Time-resolved, 2-D simulations are performed for the HF deterrent. Figure 14 shows a visualization of the radiating acoustic field via instan-

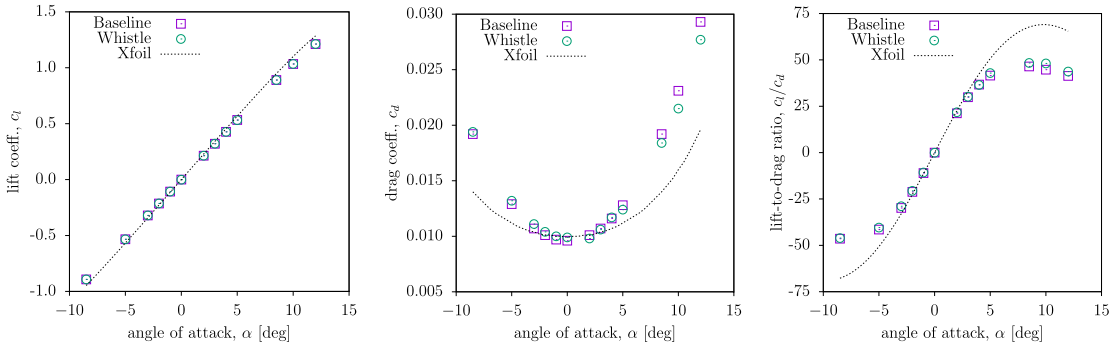

(a) lift coefficient, c_l (b) drag coefficient, c_d (c) lift-to-drag ratio

Fig. 12. CFD predictions of the lift and drag coefficients and lift-to-drag ratio. XFOIL predictions are shown for reference.

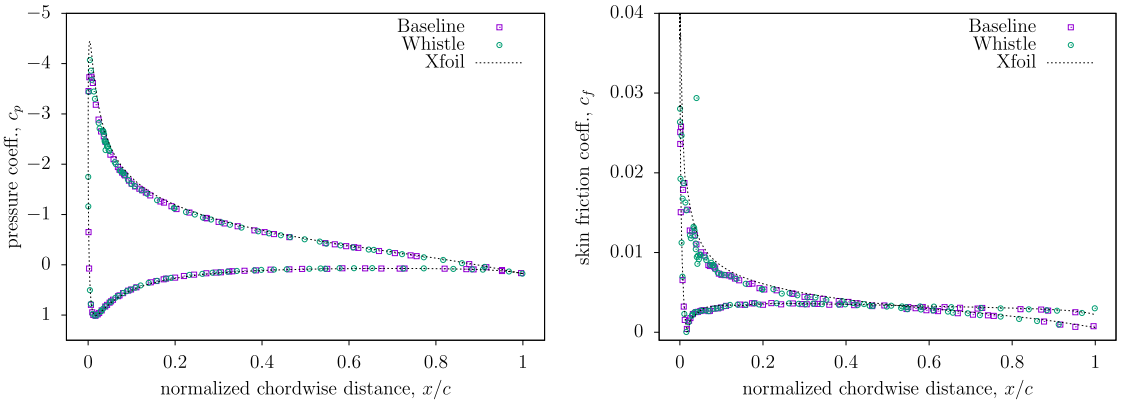

(a) Pressure coefficient, c_p (b) Skin friction coefficient, c_f

Fig. 13. CFD predicted distributions of pressure and skin friction coefficients on the airfoil surface at angle-of-attack, $\alpha = 8.5°$. Also plotted for reference are XFOIL predictions.

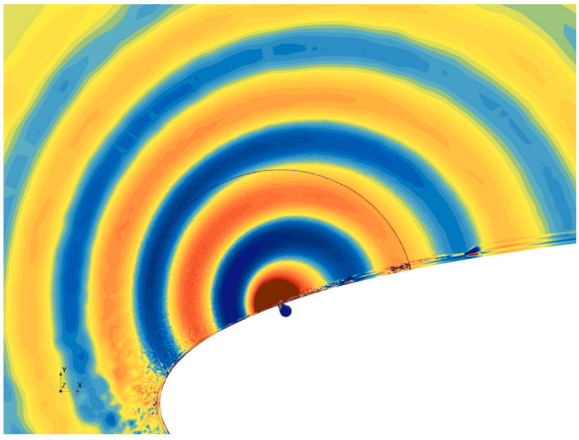

Fig. 14. Radiated acoustic field visualized with instantaneous pressure contours in a 2-D simulation of the HF deterrent.

taneous pressure contours. Strong tonal radiation originating from the resonator is observed in the figure.

Time-accurate pressure data is collected at two locations in the computational domain. One probe (Probe A) is located in the center of the resonating chamber, and another (Probe B) is located 10 mm away from the chamber opening. Fourier analysis of the pressure time history at Probe B is performed to generate the power spectral density (PSD) of the signal. Figure 15b presents a qualitative comparison of the pressure PSD spectra between the 2-D predictions and measurements. The ordinate values are not shown in the figure as they are irrelevant; the measurements are made in the acoustic farfield where the acoustic waves radiate in a 3-D space, whereas the numerical result is a 2-D prediction (radiation restricted to a 2-D space) at a point close to the airfoil. The numerical prediction captures the measured frequencies of the fundamental tone and the second harmonic.

5.2.1. *Variation with flow speed*

Two-dimensional simulations are conducted for V_∞ values ranging from 21 m/s to 96 m/s for both HF and LF deterrents. A Fourier analysis of the unsteady pressure signal at Probe A (located at the center of the resonating chamber) is performed to identify the peak radiation frequency. Figure 16 illustrates the variation of peak frequencies with V_∞ for the two deterrents. The figure also presents experimental data and theoretical estimates for the Helmholtz resonance frequency and the first Rossiter mode frequency.

Resonance occurs when the freestream flow speed, V_∞, exceeds the onset speed ($V_{\infty,\min}$). The onset of oscillations/resonance is observed in both simulations and experiments (Figs. 7 and 16). We also identify an upper limit on V_∞ beyond which oscillations do not occur in our simulations (Figs. 16a and 16b). This phenomenon was observed by Mongeau et al. [50] in their measurements of pressure oscillations in scaled models of passenger cars. While the theoretical model of Covert [51] does not predict this upper limit due to their inviscid flow assumption, they state that there is experimental evidence for oscillations ceasing as velocity exceeds a critical maximum value. $V_{\infty,\max}$ was not reached in our experiments due to the tunnel's maximum safe operating speed limit of 60 m/s.

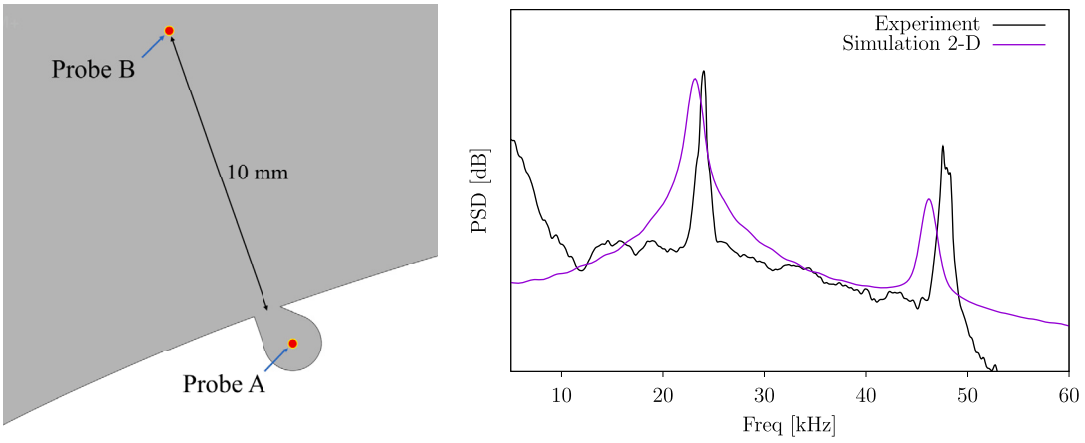

(a) Probe locations (b) PSD spectra

Fig. 15. Sample 2-D CFD simulation: (a) locations where time accurate data is sampled, and (b) a qualitative comparison of the radiated acoustic spectra between 2-D CFD (Probe B) and experiments ($V_\infty = 60$ m/s, $\alpha = 0°$).

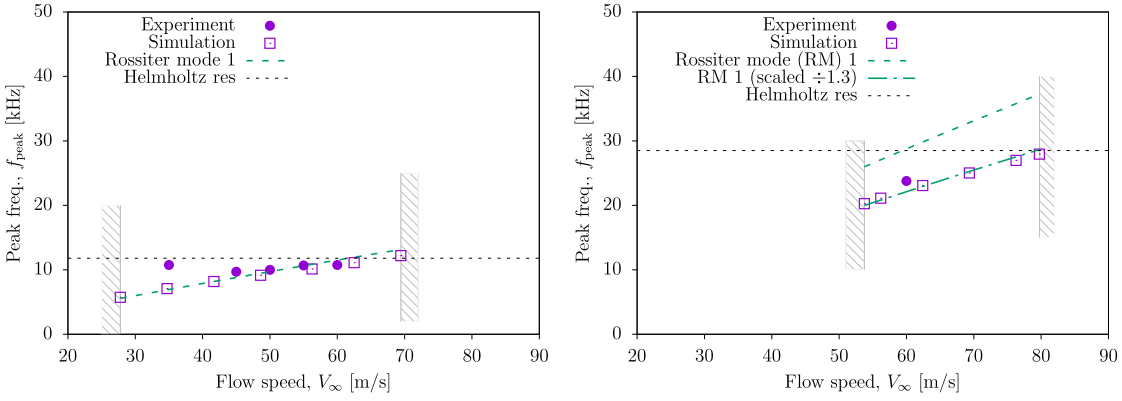

(a) LF (b) HF

Fig. 16. Variation of the peak (fundamental) frequency with V_∞ for the LF (a) and HF (b) deterrents. The gray hashed regions indicate the lower and upper limits on V_∞ beyond which acoustic radiation does not occur. The solid lines show the 2-D CFD simulation predictions while the hollow circles show the measured data. The dotted horizontal line shows the estimated (theoretical) Helmholtz resonance frequency, and the green dashed line shows the first Rossiter mode frequency for the deterrent based on freestream velocity. The label 'RM 1 (scaled)' refers to the Rossiter mode frequency scaled by 1.3 to compare the trend.

In the V_∞ range where acoustic radiation occurs, the fundamental frequency is predicted to increase almost linearly with V_∞, closely matching the theoretical estimate for the first Rossiter mode frequency. The rate of increase is greater for the HF deterrent compared to the LF deterrent. While the Helmholtz resonance frequency remains constant, the frequency of the Rossiter mode varies linearly with flow speed above the cavity. In the case of spatially varying mean flow, it is uncertain at which point the flow speed should be evaluated. Here, the freestream flow speed, V_∞, is used, which works well for the LF deterrent but needs to be scaled down by a factor of 1.3 for the HF deterrent to align with the CFD simulations. The measured data for the LF deterrent follows the linear trend predicted by CFD (Fig. 16a), except at $V_\infty = 35$ m/s. There are competing resonance mechanisms - Helmholtz and Rossiter modes. At this flow speed, the system appears to lock into Helmholtz resonance in the experiments, while simulations indicate that the Rossiter mode mechanism dominates. For the HF deterrent, measurements are only available at $V_\infty = 60$ m/s, and this data point aligns with the CFD-predicted trend line, consistent with the theoretical estimate of the first Rossiter mode frequency (Fig. 16b).

5.2.2. *Variation with angle-of-attack*

The acoustic performance of the HF deterrent is numerically investigated for α values ranging from −8.5° to 12°, with experimental data available at $\alpha = 0°, 2°, 4°$. Similar to $V_{\infty,\min}$, there is a minimum α ($\alpha_{\min} = -1°$) below which acoustic radiation does not occur. The fundamental frequency at $\alpha_{\min}$ is 20.3 kHz, the same frequency observed at $V_{\infty,\min}$ (Fig. 16). For $\alpha < \alpha_{\min}$, the local flow speed at the deterrent location is below the onset speed. Therefore, the limits on α stem from the constraints on flow speed that determine whether resonance is excited. The maximum α for which radiation is observed in the simulations is $\alpha_{\max} = 12°$. Note that this only applies to simulations where the resonator is modeled solely on the suction side of the airfoil.

Figure 17 shows that the predicted peak frequency increases with α. This may be due to the increase in local flow velocity with α in the linear $C_l - \alpha$ range (small α). The variation of the first Rossiter mode frequency is also plotted, showing a linear increase with α; scaling it by 1.5 still indicates a much larger increase with α than in the simulations. Since the freestream velocity, V_∞ does not change with α, we use the edge velocity (derived from inviscid XFOIL calculations) to compute the Rossiter mode frequency. The discrepancy between the variations of the Rossiter mode frequency and the CFD predictions suggests that the inviscid edge velocity may not be the appropriate velocity scale, and that the velocity at a point in the boundary layer might be more suitable. The measured data roughly aligns with the CFD predicted trend; however, the variation with α is even smaller in the experiments.

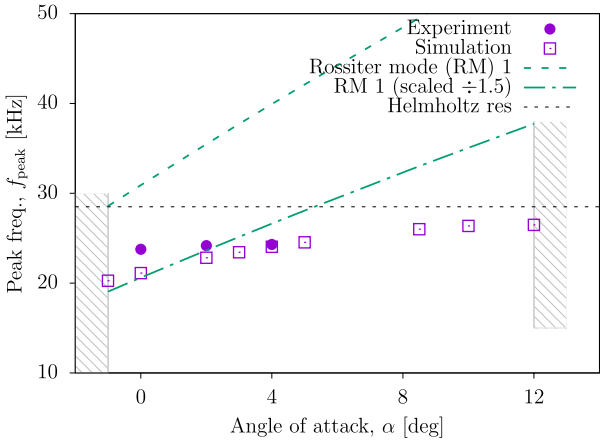

Fig. 17. Peak frequency (f_{peak}) variation with angle-of-attack (α); theoretical estimate of the Helmholtz resonance frequency, f_R is shown as the horizontal dashed line. The hashed regions bound the range of α over which acoustic radiation is predicted.

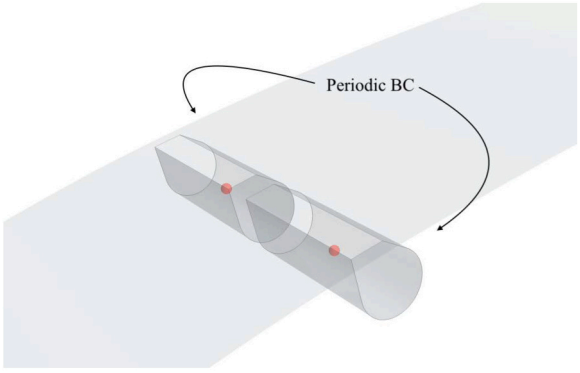

Fig. 18. An isometric view of the two-resonator computational model. Periodic boundary conditions are used in the span direction. The red points are data probes placed at the center of each resonator in the numerical model. Time-accurate pressure data is collected at these probe locations.

The resonators were engraved on both sides of the sleeve (blade) in the experimental model. An increase in α results in an increase in the local flow velocity for the resonators on the suction side of the blade but a reduction for the resonators on the pressure side. A consequence of this would be an increase in the resonance frequency of the resonators on the suction side and a reduction for the resonators on the pressure side, resulting in two peaks relatively close (in frequency) to each other. This can be observed for the LF deterrent in Fig. 8b, where the frequency separation is larger than the filter width. The two-peak pattern is unclear for the HF deterrent (Fig. 8a) because the pressure-side resonators fall below α_{min} and are unable to establish resonance.

5.3. Three-dimensional analysis

While the two-dimensional simulations provide valuable qualitative insights and design guidance, they cannot be quantitatively compared with experimental data. Therefore, three-dimensional (3-D) simulations are conducted to validate the predictions. The 3-D mesh is generated by extruding the 2-D mesh along the span. Each deterrent is simulated in two configurations: in the first configuration, one resonator is modeled, while in the second configuration, two resonators are modeled. The computational domain spans from $z = -3$ mm to $+3$ mm for the one-resonator configuration and from $z = -6$ mm to $+6$ mm for the two-resonator configuration. Periodic boundary conditions are applied in the z direction for both models; the boundary conditions on the other surfaces are consistent with those used in the 2-D simulations. Figure 18 shows an isometric view of the two-resonator numerical model. As in the 2-D simulations, the deterrent is modeled only on the suction side of the airfoil.

Given the focus on ultrasound radiation, only the results for the HF deterrent at $V_\infty = 60$ m/s are discussed. Figure 19a compares the PSD spectra of the predicted pressure signal at the center of the resonator (Probe A) for the one-resonator (1R), two-resonator (2R), and 2-D simulations. The spectrum from the 2-D simulation is similar to the 3-D prediction for the 1R model. In contrast, the 3-D simulation result for the 2R model exhibits higher signal power for both broadband and tonal sounds, with a higher peak frequency (fundamental) as well.

Analysis of the pressure time signal (Fig. 19b) for the 2R model reveals that the pressures at the centers of the two resonators are nearly out of phase. This out-of-phase relationship between resonators was also observed in our previous work on aerodynamic ultrasonic whistles powered by compressed air [35,37]. The out-of-phase oscillation between adjacent resonators enhances their response, leading to greater amplification of unsteadiness; as a result, the PSD spectrum for the 2R configuration is approximately 20 dB greater than that of the 1R configuration. It is important to note that these spectra represent the hydrodynamic pressure measured at the center of a resonator, not the radiating acoustic pressure.

Far-field ultrasound radiation is computed by solving the FW-H equation. The FW-H integration (Kirchoff) surface is illustrated in Fig. 5; it extends through the entire computational domain in the span direction. Since the deterrent span in the simulation is smaller than in the experiments, corrections have to be applied to the predicted noise radiation in order to compare with the measurements; Appendix D explains how these corrections are obtained and the approximations that are involved. Figure 20 shows the locations of the observers where the radiated acoustic field is predicted. These observer locations are arranged in a line (array) parallel to the blade leading edge (along z) and range from $z = -144$ mm to $+144$ mm. This range corresponds to the span over which the resonators are positioned on the deterrents (HF and LF) tested in the wind tunnel.

The center of the observer array is located at a 90° polar angle (measured from upstream) and is 1 m directly above the suction side of the blade leading edge, aligning with the center of the microphone array used in the experiments. For the 1R model, the distance between adjacent observers is 6 mm, which matches the span of the numerical model. The 2R model has double the span, so the observers are spaced 12 mm apart. By summing (with appropriate phases) the predicted sound signals at all observer locations along each array, we obtain the signal that would be measured at the center observer location for the full-size deterrent (with a 288 mm span) (see Appendix D).

We first examine the farfield pressure PSD spectra predictions without span correction. The simulated spans are 6 mm for the 1R configuration and 12 mm for the 2R configuration. Farfield acoustics is compared at the observer located 1 m away at a 90° polar angle (see Figs. 20a and 21a). The result for the one-resonator model appears as expected, with the fundamental resonance frequency peak exhibiting higher intensity than the second harmonic. In contrast, the second harmonic for the 2R model is stronger than the fundamental, despite the hydrodynamic pressure inside the resonator showing greater intensity at the fundamental frequency (Fig. 19a). This discrepancy arises because the unsteady pressures in the two resonators in the 2R model are out of phase (Fig. 19b), resulting in partial cancellation of the radiated sound for the odd harmonics of the fundamental frequency.

The 2R simulation clearly demonstrates a strong correlation between adjacent resonators. However, the degree of correlation between the 48 resonators across the entire span of the physical deterrent is unknown. To address this, we make two assumptions for our far-field predictions: (1) all resonators in the deterrent are completely correlated, and (2) the resonators are completely uncorrelated. We hypothesize that these two assumptions bound the actual far-field acoustic intensity.

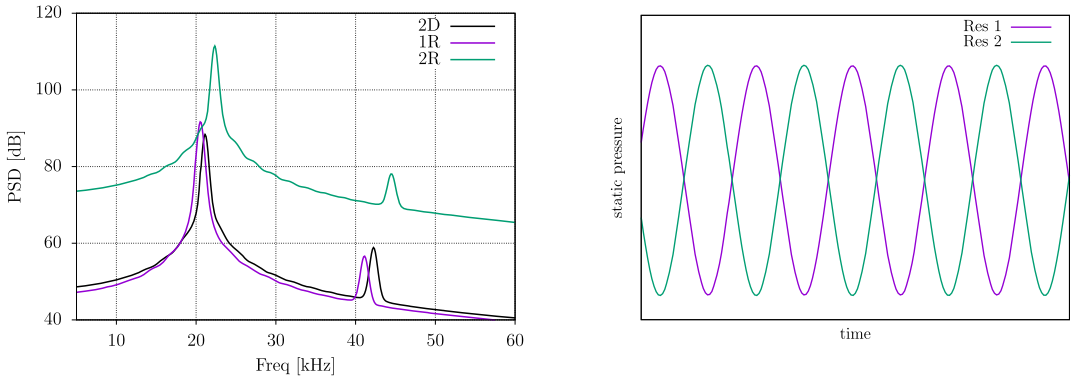

(a) PSD spectra (b) pressure time signals

Fig. 19. PSD spectra at the resonator chamber center compared between different simulations (a), and time history of pressure measured at the centers of the two resonators in the two-resonator simulation.

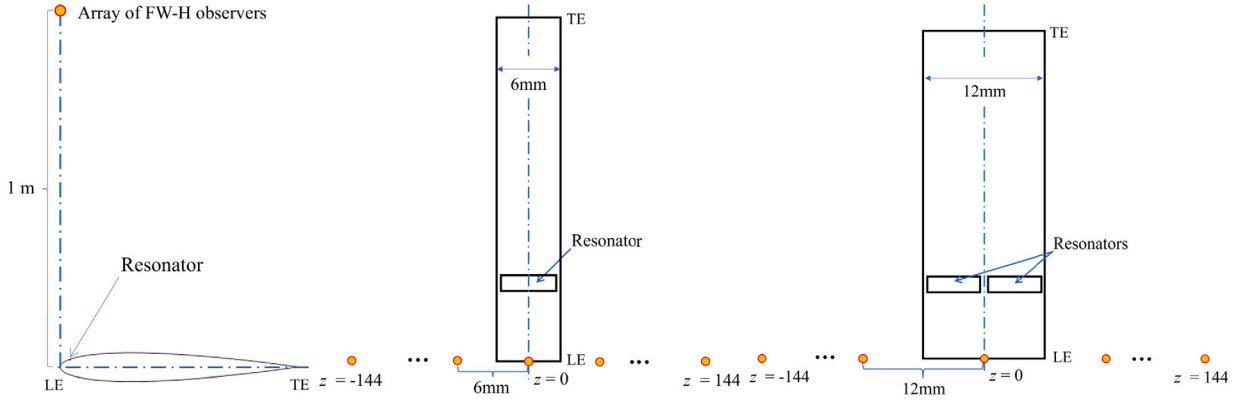

(a) Side view (b) Top view: one-resonator config (c) Top view: two-resonator config

Fig. 20. Observer locations: (a) side view showing that the observer array is located at 90° polar angle, (b & c) top views of the one-resonator and two-resonator models; the array of observers spans $z = -144$ mm to $+144$ mm, and the spacing between adjacent operators is equal to the span of the blade simulated (= 6 mm and 12 mm for one- and two-resonator models respectively).

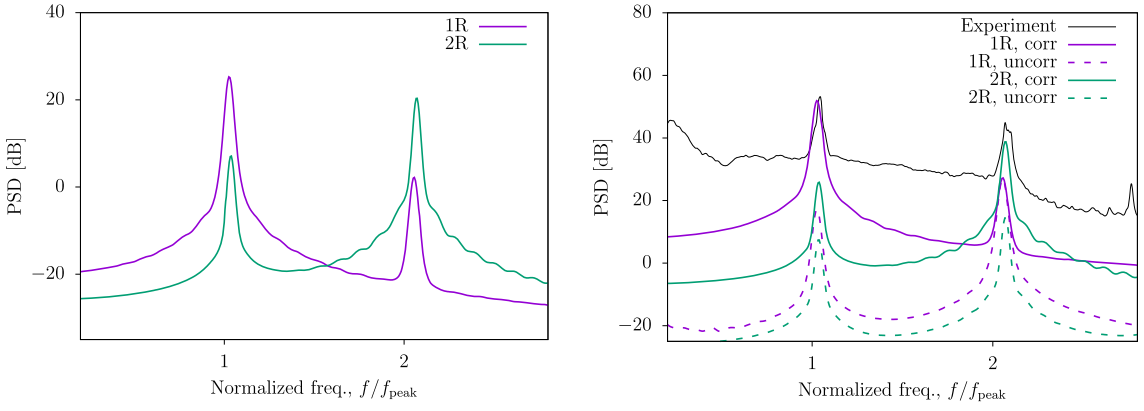

(a) Partial span (1R: 6 mm & 2R: 12 mm) predictions (b) Experiment and full-span predictions

Fig. 21. Predicted PSD spectra for the HF deterrent at the observer located 1 m directly above the airfoil leading edge (90° polar angle). (a) Predictions from the 6 mm-span one-resonator configuration (1R) and 12 mm-span for the two-resonator configuration (2R), and (b) experimental data and predictions for the full-span (288 mm) HF deterrent for the two configurations. For the full-span predictions, the signals from the different resonators are assumed to be fully correlated (solid lines) and completely uncorrelated (dashed lines).

Table 3
Sound pressure level (SPL wref 20μpa) values for the fundamental and the second harmonic for the HF deterrent and atmospheric attenuation at those frequencies. Predictions are made using two assumptions: full correlation across the resonators and zero correlation across the resonators for the 1R case. Tonal SPL values are obtained by integrating the pressure PSD spectra over frequency bands around the tones.

Frequency [kHz]	Experiment [dB]	Prediction [dB]				Atm. abs. [dB/m]
		Correlated	Uncorrelated	Mean	Error	
20.5	78.98	98.37	63.72	81.05	±17.33	0.55
41.0	72.77	70.12	70.14	70.13	±0.01	1.36

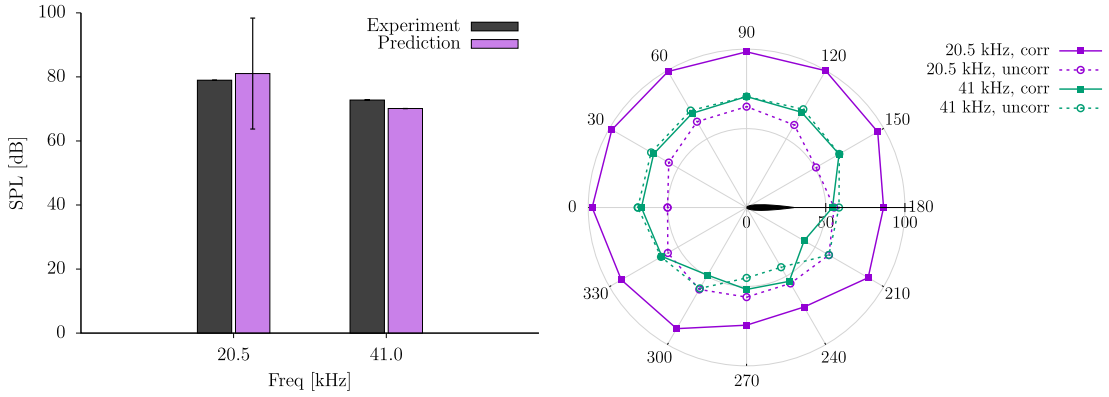

(a) Tone SPLs (b) Polar directivity

Fig. 22. Numerical predictions of the farfield (1 m) sound pressure levels (SPLs) of the fundamental (20.5 kHz) and the second harmonic (41 kHz) corrected for atmospheric absorption. The SPLs are obtained by integrating the PSD spectra over a frequency band (2 kHz for simulations and 1.6 kHz for experiments) around each tone. (a) SPL comparison for the fundamental tone and the second harmonic at 90° polar angle between measurements and numerical prediction for the HF deterrent (one-resonator configuration) at $V_\infty = 60$ m/s and $\alpha = 0°$. The predicted SPLs are the average of the results obtained by assuming full correlation and zero correlation across the resonators; the error bar denotes the difference between the two. (b) Predicted directivity patterns assuming the resonators are completely correlated (solid) and completely uncorrelated (dashed).

Figure 21b compares the predicted spectra from the full-span (288 mm) deterrent at the observer 1 m away at a 90° polar angle. The broadband noise cannot be directly compared, as the major source of this noise is airfoil self-noise, which is not included in the simulations. At first glance, it seems that the peak PSD at the fundamental frequency is well predicted by the 1R model when assuming complete correlation. However, it is important to note that the frequency bandwidths of the spectral peaks differ between the experiments and predictions. A more relevant metric for tonal sound is the tonal sound pressure level (SPL), obtained by integrating the PSD over the frequency band that defines the tone. SPLs are compared in Table 3 and Fig. 22a, indicating that the fully-correlated assumption is inaccurate.

Assuming that the resonators are completely decorrelated leads to a reduction in PSD for both tones in the 2R case, but only for the fundamental tone in the 1R case. This can be attributed to phase cancellation occurring in the one-resonator case for the fundamental tone, stemming from the different source-to-observer distances for the various observer locations.

The SPLs of the fundamental and the second harmonic for the 1R case are compared with the measurements in Table 3 and in Fig. 22a. The predicted results are shown as mean values with error bars, where the mean value is the average of the two SPLs obtained using the completely correlated and the completely uncorrelated assumptions, and the error bar is the difference between the two. The predicted results have been corrected for atmospheric absorption; the corrections are given in Table 3. Figure 22a suggests that the resonators in the deterrent are partially correlated. Figure 22b shows the predicted SPL directivity patterns for the fundamental and the second harmonic. The deterrent is only on the suction side in the simulations. Hence, the radiation intensity is high ahead of and above the blade.

6. Conclusions

This paper introduces a novel, passive, blade-mounted bat deterrent for wind turbines and presents a comprehensive computational and experimental investigation of its acoustic characteristics and impact on the blade's aerodynamic performance. The deterrent is based on the concept of aerodynamic whistles. It uses resonating cavities that are placed near the leading edge of the blade. Two designs are considered: a low-frequency deterrent (LF) and a high-frequency deterrent (HF). The HF deterrent is a geometrically scaled-down version of the LF deterrent. The Helmholtz resonance frequencies of the LF and HF deterrents are approximately 10 kHz and 20.5 kHz respectively.

The experiments were conducted in the Virginia Tech Stability Wind Tunnel where acoustic measurements were made with an acoustic array mounted on the Starboard side wall of the tunnel. In line with the existing literature on cavity noise, the measurements indicate that there is a minimum flow speed ($V_{\infty,\min}$) below which the deterrents do not produce sound. $V_{\infty,\min}$ is a function of the deterrent geometry; it lies between 55 and 60 m/s for the HF deterrent and between 30 and 35 m/s for the LF deterrent. The peak radiation frequency and the radiated acoustic intensity increase slightly with V_∞. A small increase in radiated acoustic intensity is also observed with blade angle of attack (α) due to the increase in local flow speed over the deterrent.

Numerical simulations are performed in two and three dimensions using the uRANS model. The simulations confirm the presence of a deterrent-specific onset flow speed and also reveal that there is a $V_{\infty,\max}$ beyond which resonance does not take place. The peak frequency increases linearly with V_∞, which aligns with the theoretical estimate of the first Rossiter mode frequency. A slight increase in peak frequency is also observed with α. The predicted trends with V_∞ and α agree with the measurements. Three-dimensional simulations are performed

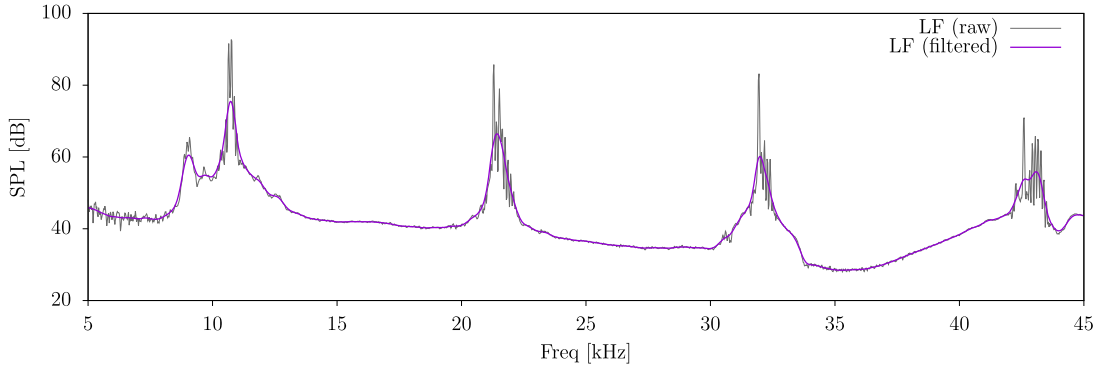

Fig. 23. Integrated beamforming sound pressure level (SPL) spectra. The raw signal (gray) shows multiple sharp peaks around each expected tone; the Gaussian-filtered signal (purple) shows the expected spectral broadening of tones due to differences in the geometry of the resonators.

to quantitatively compare the predictions with the experiments. Two configurations are considered - one modeling a single resonator and the other modeling two resonators, both with spanwise periodic boundaries. The results show that the unsteady pressures in the resonators of the two-resonator configuration are nearly out of phase, with each resonator exhibiting significantly higher unsteadiness than the one-resonator configuration. The out-of-phase behavior, however, leads to partial cancellation of the odd harmonics in the radiated sound.

Acoustic propagation is performed by solving the Ffowcs Williams and Hawkings equation. The one-resonator configuration is used for farfield prediction. Since the simulations use a smaller span than the deterrents used in the experiments, two sets of farfield predictions are made with the following assumptions regarding the degree of correlation between the resonators: (1) 100% correlation and (2) 0% correlation. The tonal SPLs predicted using these two methods are expected to bound the measured values. The overall agreement with the measured data is modest. Tonal directivity shows the highest intensity directly upstream of the blade and the lowest on the downstream pressure side.

CRediT authorship contribution statement

Zhangming Zeng: Writing – original draft, Visualization, Validation, Investigation, Formal analysis, Data curation. **Szu-Fu Huang:** Visualization, Investigation, Data curation. **William N. Alexander:** Writing – review & editing, Methodology, Investigation. **Anupam Sharma:** Writing – review & editing, Investigation, Funding acquisition, Conceptualization.

Declaration of competing interest

The authors declare the following financial interests/personal relationships which may be considered as potential competing interests:

Anupam Sharma reports financial support was provided by US Department of Energy. Anupam Sharma reports financial support was provided by National Science Foundation. If there are other authors, they declare that they have no known competing financial interests or personal relationships that could have appeared to influence the work reported in this paper.

Acknowledgements

This material is based upon work supported by the U.S. Department of Energy Office of Energy Efficiency and Renewable Energy (EERE) under the Wind Energy Technologies Office Award Number DE-EE0008731 and DE-EE0011086. The National Science Foundation (Grants CBET-1554196 and 1935255) also partially supported this research. We also acknowledge the computational resources provided by the Department of Defense through the US Air Force Office of Scientific Research (Award # FA9550-23-1-0016) and the Iowa State University.

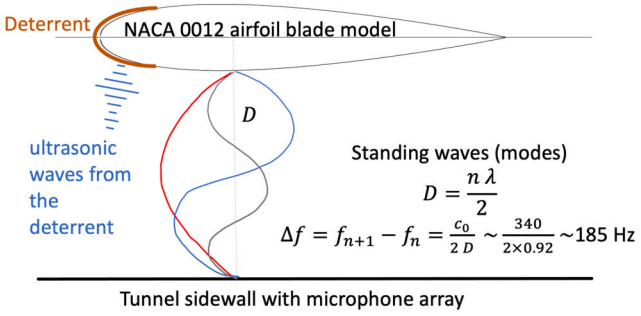

Fig. 24. An illustration of standing waves between the airfoil/blade model and the hard sidewall of the tunnel on which the microphone array is installed.

Appendix A. Standing waves in the stability wind tunnel

The measured spectra in the Stability Wind Tunnel show several sharp peaks above the broad peaks at the frequencies corresponding to the resonance frequencies of the whistle/deterrent (see the gray curve in Fig. 23). A Gaussian filter is applied to the signal to reveal the spectrally broadened peaks that can be expected due to slight geometric differences between the resonators in a deterrent, each resonator having a slightly different resonance frequency.

We hypothesize that these additional sharp peaks are due to standing waves/modes trapped between the blade model and the hard sidewall of the tunnel on which the beamforming array is mounted. Figure 24 illustrates this phenomenon. The channel between the blade and the hard sidewall can act as a waveguide, amplifying the acoustic modes supported by the hard-wall boundary conditions. Assuming hard-wall boundary conditions at both ends (blade surface and tunnel sidewall) and ignoring the blade thickness, the expected frequency gap, Δf, between these tones is approximately 185 Hz assuming the speed of sound, $c_0 = 340$ m/s. The measured data shows frequency shifts that are integer multiples of this Δf, suggesting that multiple modes ($n = 1, 2, \ldots$) are excited.

Appendix B. Beamform maps for the HF deterrent

The imprecise determination of source locations in the beamform maps shown in Figs. 9 and 10 is investigated further through simulation. We note that the tightly spaced resonators could have coupled end conditions at their openings, which establish a fixed phase condition between the tonal pressure sources. The effect of this coupling on the beamform maps is investigated by simulating a distribution of monopole sources similar to the LF and HF deterrents with in-phase and out-of-phase resonance of adjacent sources. The coordinate system is such that the simulated sources are distributed in the vertical direction about $x = y = 0$. Each monopole source is located at the center

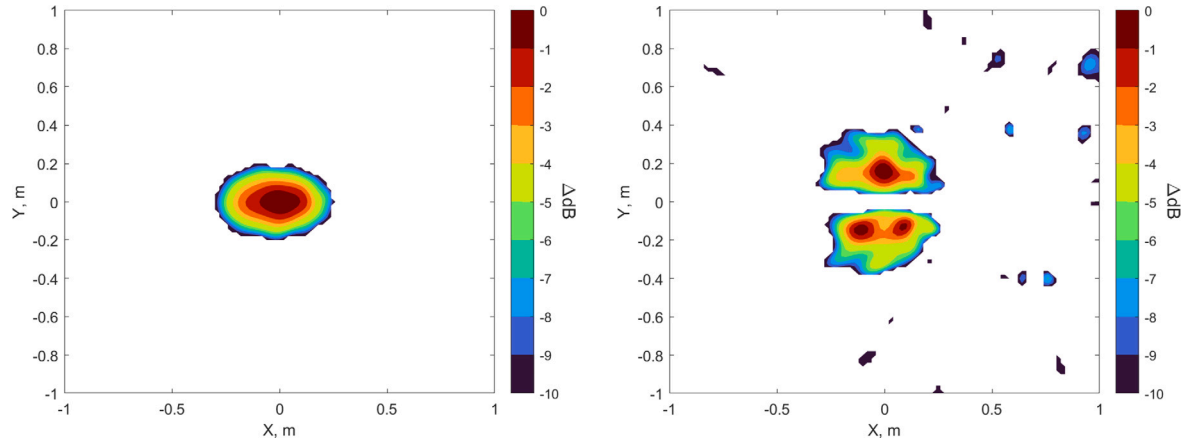

Fig. 25. Simulated beamform maps of the LF deterrent at 10.6 kHz with adjacent resonators a) in-phase b) and 180° out-of-phase.

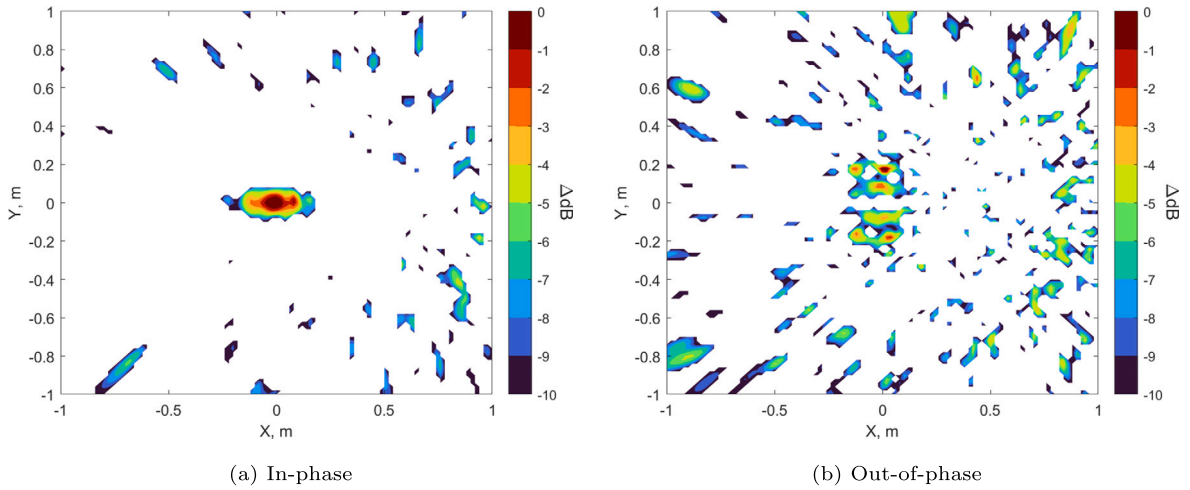

Fig. 26. Simulated beamform maps of the HF deterrent at 23.6 kHz with adjacent resonators a) in-phase b) and 180° out-of-phase.

of each resonator from the experimental measurements extending from $y = -0.1346$ m to 0.1346 m. The relative locations of the microphones are matched to the positions in the measurement.

Two frequencies are analyzed. The beamform maps produced by simulation of the LF deterrent at a resonant frequency of 10.6 kHz are shown in Fig. 25. Similarly, results for the HF deterrent at a resonant frequency of 23.6 kHz are shown in Fig. 26. For both deterrents, the map shows a single peak at the center of the deterrent locations if all resonators are assumed to be in phase. When adjacent resonators are 180° out-of-phase, the source distribution becomes more complex. For the LF deterrent, peaks appear near the bottom and top of the deterrent location. The HF deterrent produces a beamform map with strong scattered sidelobes that is not a reflection of the correct source distribution. The results shown in the out-of-phase calculations are similar to the experimental results. Although the true phase between resonators for both deterrents in the experimental measurements is unknown and most likely lies between these two extremes, this analysis suggests that the phase between the distributed tonal sources can produce the ambiguous beamform maps presented in Figs. 9 and 10.

Appendix C. Mesh sensitivity study

A study on spatial and temporal mesh refinement was conducted for the two-dimensional configuration. Favorable comparisons with XFOIL (Fig. 12) confirmed the accuracy of the boundary layer flow simulation over the airfoil using the baseline mesh. Consequently, only the mesh in and around the resonator was modified to ensure mesh independence in the acoustic results. Four mesh types were created – Coarse, Baseline, Fine, and Finest – and two time step sizes were evaluated for the baseline mesh (see Table 4). As shown in Fig. 27, the pressure power pred at the center of the resonator is nearly independent of mesh size beyond the baseline mesh, and a time step of $\Delta t = 2.5E-07$ is sufficient. The findings of the study are summarized in Fig. 27.

Table 4
Test cases for mesh refinement study. Δx_{base} is the approximate mesh size (estimated as cube-root of cell volume) in the resonator.

Name	$\Delta x/\Delta x_{base}$	Δt (in s)
Coarse	1.50	2E-07
Baseline	1.00	2.5E-07, 5.0E-07
Fine	0.75	2.5E-07
Finest	0.50	2.5E-07

Appendix D. Noise prediction using small-span simulations

Computational cost increases proportionately with domain size in fluid flow simulations. Span periodicity is typically employed to reduce the domain size. If there is physical periodicity in the span direction,

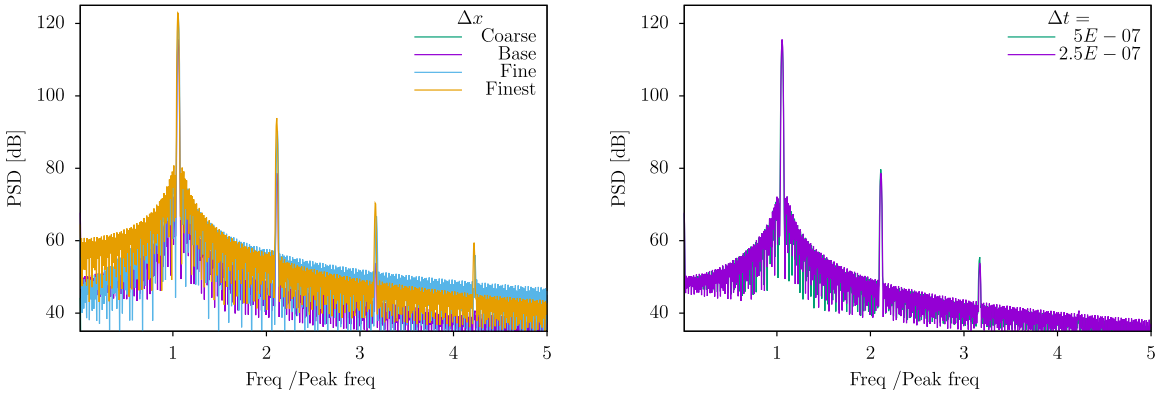

(a) mesh spacing sensitivity (b) time step sensitivity

Fig. 27. Results from a mesh refinement study: (a) mesh spacing, Δx, and (b) time step, Δt. The power spectral density spectra correspond to the unsteady pressure at the center of the resonator.

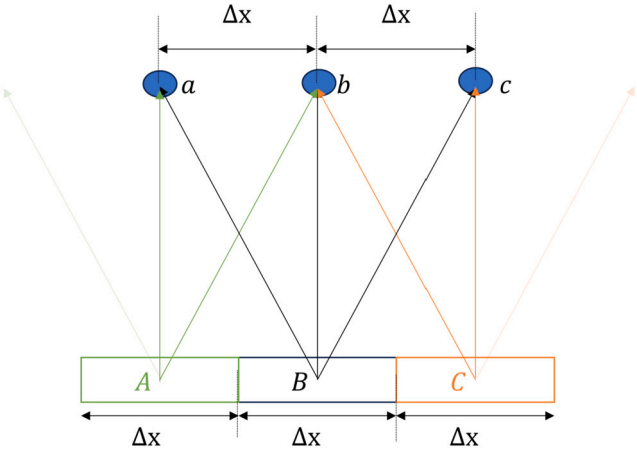

Fig. 28. A schematic to explain how a small-span-deterrent simulation result is used to predict noise from the full-scale deterrent.

and the full span is simulated, then the boundary condition replicates reality. Otherwise, the numerically imposed periodicity introduces some artifacts in the solution [52]. Depending on the spanwise coherence of the problem, these artifacts can be negligible. Consider the schematic in Fig. 28 where B is the computational model with a span of Δx, which is a third of the span of the physical model made up of blocks A, B, and C. Say our interest is computing the noise from the physical model at observer location b. Denote the radiated acoustic pressure from block B at observer location b by $p_{B\to b}$. Similarly, the radiated acoustic pressure from A to b and C to b is $p_{A\to b}$ and $p_{C\to b}$ respectively.

The numerical model uses spanwise periodicity. Hence, in the numerical solution, A and C are replicas of B. If the sources in A, B, and C are fully correlated, then the noise at observer b from the full physical model is

$$p_b = p_{A\to b} + p_{B\to b} + p_{C\to b}. \tag{8}$$

If the sources are totally uncorrelated, then

$$p_b^2 = p_{A\to b}^2 + p_{B\to b}^2 + p_{C\to b}^2. \tag{9}$$

Because of the relative distances and the radiation angles involved, and the fact that the numerical solution in A, B, and C are identical, $p_{A\to b}$ is identical to $p_{B\to c}$, and $p_{C\to b}$ is identical to $p_{B\to a}$. These relations can be used with Eqs. (8) and (9) to write

$$p_b = p_{B\to c} + p_{B\to b} + p_{B\to a}, \quad \text{(completely correlated)}$$

$$p_b^2 = p_{B\to c}^2 + p_{B\to b}^2 + p_{B\to a}^2 \quad \text{(completely uncorrelated)}. \tag{10}$$

Equation (10) shows that the noise from the full physical model at observer b can be obtained by appropriately adding the noise from the simulation of a smaller model (B) at multiple observer locations (a, b, and c) that are spaced the model span length (Δx) apart. The example here uses three blocks but can be extended to an arbitrary number of blocks. The spanwise periodicity assumption is invalid if the sources are partially correlated. However, one can approximate that the actual noise would lie between the two predictions obtained assuming zero and full correlation.

Data availability

Data will be made available on request.

References

[1] Rosenberg A, Selvaraj S, Sharma A. A novel dual-rotor turbine for increased wind energy capture. J Phys Conf Ser 2014;524:012078.
[2] Hu H, Wang Z, Ozbay A, Tian W, Sharma A. An experimental investigation on the wake characteristics behind a novel twin-rotor wind turbine. In: 33rd wind energy symposium; 2015. p. 1663.
[3] Moghadassian B, Rosenberg A, Sharma A. Numerical investigation of aerodynamic performance and loads of a novel dual rotor wind turbine. Energies 2016;9:571.
[4] Rosenberg A, Sharma A. A prescribed-wake vortex lattice method for preliminary design of co-axial, dual-rotor wind turbines. J Sol Energy Eng 2016;138.
[5] Moghadassian B, Sharma A. Inverse design of single- and multi-rotor horizontal axis wind turbine blades using computational fluid dynamics. J Sol Energy Eng 2018;140.
[6] Moghadassian B, Sharma A. Designing wind turbine rotor blades to enhance energy capture in turbine arrays. Renew Energy 2020;148:651–64.
[7] Chen L, Harding C, Sharma A, MacDonald E. Modeling noise and lease soft costs improves wind farm design and cost-of-energy predictions. Renew Energy 2016;97:849–59.
[8] Cryan PM. Wind turbines as landscape impediments to the migratory connectivity of bats. J Environ Law 2011:355–70.
[9] Cryan PM, Brown AC. Migration of bats past a remote island offers clues toward the problem of bat fatalities at wind turbines. Biol Conserv 2007;139:1–11.
[10] O'Shea TJ, Cryan PM, Hayman DT, Plowright RK, Streicker DG. Multiple mortality events in bats: a global review. Mammal Rev 2016;46:175–90.
[11] Smallwood KS. Comparing bird and bat fatality-rate estimates among North American wind-energy projects. Wildl Soc Bull 2013;37:19–33.
[12] Voigt CC, Lehnert LS, Petersons G, Adorf F, Bach L. Wildlife and renewable energy: German politics cross migratory bats. Eur J Wildl Res 2015;61:213–9.
[13] Arnett EB, Baerwald EF. Impacts of wind energy development on bats: implications for conservation. In: Bat evolution, ecology, and conservation. Springer; 2013. p. 435–56.
[14] Hayes MA. Bats killed in large numbers at United States wind energy facilities. Bioscience 2013;63:975–9. https://doi.org/10.1525/bio.2013.63.12.10.
[15] Zimmerman R. Biologists struggle to solve bat deaths. Science 2009;324:1134–5. https://doi.org/10.1126/science.324_1134.
[16] Frick WF, Kingston T, Flanders J. A review of the major threats and challenges to global bat conservation. Ann NY Acad Sci 2020;1469:5–25.

[17] Friedenberg NA, Frick WF. Assessing fatality minimization for hoary bats amid continued wind energy development. Biol Conserv 2021;262:109309.
[18] Cheng TL, Reichard JD, Coleman JT, Weller TJ, Thogmartin WE, Reichert BE, et al. The scope and severity of white-nose syndrome on hibernating bats in North America. Conserv Biol 2021;35:1586–97.
[19] Baerwald EF, Edworthy J, Holder M, Barclay RM. A large-scale mitigation experiment to reduce bat fatalities at wind energy facilities. J Wildl Manag 2009;73:1077–81.
[20] Arnett EB, Hein CD, Schirmacher MR, Huso MM, Szewczak JM. Evaluating the effectiveness of an ultrasonic acoustic deterrent for reducing bat fatalities at wind turbines. PLoS ONE 2013;8.
[21] Martin CM, Arnett EB, Stevens RD, Wallace MC. Reducing bat fatalities at wind facilities while improving the economic efficiency of operational mitigation. J Mammal 2017;98:378–85.
[22] Romano WB, Skalski JR, Townsend RL, Kinzie KW, Coppinger KD, Miller MF. Evaluation of an acoustic deterrent to reduce bat mortalities at an Illinois wind farm. Wildl Soc Bull 2019;43:608–18.
[23] Weaver SP, Hein CD, Simpson TR, Evans JW, Castro-Arellano I. Ultrasonic acoustic deterrents significantly reduce bat fatalities at wind turbines. Glob Ecol Conserv 2020;24:e01099.
[24] Gorresen PM, Cryan PM, Dalton DC, Wolf S, Johnson JA, Todd CM, et al. Dim ultraviolet light as a means of deterring activity by the Hawaiian hoary bat lasiurus cinereus semotus. Endanger Species Res 2015;28:249–57.
[25] Huzzen B. Does a textured coating alter bat activity and behavior in proximity to wind turbine towers? Ph.D. thesis. Texas Christian University; 2019.
[26] Good RE, Iskali G, Lombardi J, McDonald T, Dubridge K, Azeka M, et al. Curtailment and acoustic deterrents reduce bat mortality at wind farms. J Wildl Manag 2022;e22244.
[27] Schirmacher MR. Evaluating the effectiveness of an ultrasonic acoustic deterrent in reducing bat fatalities at wind energy facilities. Technical Report. Austin, TX (United States): Bat Conservation International; 2020.
[28] Horn JW, Arnett EB, Jensen M, Kunz TH. Testing the effectiveness of an experimental acoustic bat deterrent at the maple ridge wind farm. Report prepared for: The bats and wind energy cooperative and bat conservation. Austin, TX: International; 2008.
[29] Chanaud RC. Aerodynamic whistles. Sci Am 1970;222:40–7.
[30] Rayleigh JWSB. The theory of sound, vol. 2. Macmillan; 1896.
[31] Wilson T, Beavers G, DeCoster M, Holger D, Regenfuss M. Experiments on the fluid mechanics of whistling. J Acoust Soc Am 1971;50:366–72.
[32] Gloerfelt X. Cavity noise. VKI lecture series, vol. 3. 2009.
[33] Rossiter J. Wind-tunnel experiments on the flow over rectangular cavities at subsonic and transonic speeds. Technical Report R & M No. 3438. Aeronautical Research Council, Ministry of Aviation; 1966.
[34] Bennett GJ, Stephens DB, Rodriguez Verdugo F. Resonant mode characterisation of a cylindrical Helmholtz cavity excited by a shear layer. J Acoust Soc Am 2017;141:7–18.
[35] Zeng Z, Sharma A. Aerodynamic-whistles-based ultrasonic tone generators for bat deterrence. Phys Fluids 2023;35.
[36] Sharma A, Zeng Z. Passive ultrasonic deterrents to reduce bat mortality in wind farms. Technical Report. Department of Energy; 2023.
[37] Zeng Z, Sharma A. Frequency modulation of an aerodynamic whistle-based bat deterrent. Appl Acoust 2025;228:110276.
[38] Zeng Z, Sharma A. Experimental and numerical aeroacoustic analysis of an ultrasound whistle. In: AIAA Aviation Forum; 2021.
[39] Kunz TH, Arnett EB, Erickson WP, Hoar AR, Johnson GD, Larkin RP, et al. Ecological impacts of wind energy development on bats: questions, research needs, and hypotheses. Front Ecol Environ 2007;5:315–24.
[40] Horn JW, Arnett EB, Kunz TH. Behavioral responses of bats to operating wind turbines. J Wildl Manag 2008;72:123–32.
[41] Krishnamurty K. Acoustic radiation from two-dimensional rectangular cutouts in aerodynamic surfaces. Technical Report TN 3487. National Advisory Committee for Aeronautics; 1955.
[42] Dykes K, Resor B, Platt A, Guo Y, Ning A, King R, et al. Effect of tip-speed constraints on the optimized design of a wind turbine. Technical Report NREL/TP-5000-61726. Golden, CO (United States): National Renewable Energy Lab. (NREL); 2014.
[43] Szoke M, Borgoltz A, Kuester M, Intaratep N, Ravetta P. Design and in-situ calibration of a beamforming array for high-frequency noise measurements in a hybrid-anechoic wind tunnel. In: 28th AIAA/CEAS aeroacoustics conference; 2022. p. 132.
[44] Menter FR. Two-equation eddy-viscosity turbulence models for engineering applications. AIAA J 1994;32:1598–605.
[45] ISO 9613-1:1996. Calculation of the absorption of sound by the atmosphere. Standard. International Organization for Standardization; 1995.
[46] Bass HE, Sutherland LC, Zuckerwar AJ, Blackstock DT, Hester D. Atmospheric absorption of sound: further developments. J Acoust Soc Am 1995;97:680–3.
[47] Sarohia V. Experimental and analytical investigation of oscillations in flows over cavities. Ph.D. thesis. California Institute of Technology; 1975.
[48] Gharib M, Roshko A. The effect of flow oscillations on cavity drag. J Fluid Mech 1987;177:501–30.
[49] Drela M. Xfoil: an analysis and design system for low Reynolds number airfoils. In: Low Reynolds number aerodynamics: proceedings of the conference Notre Dame. Springer; 1989. p. 1–12.
[50] Mongeau L, Brown D, Kook H, Zorea S. A predictive model for the interior pressure oscillations from flow over vehicle openings. SAE Transact 1997:2675–84.
[51] Covert EE. An approximate calculation of the onset velocity of cavity oscillations. AIAA J 1970;8:2189–94.
[52] Wu X, Sharma A. Artefacts of finite span in vortex-induced vibration simulations. Appl Ocean Res 2020;101:102265.